nature reviews methods primers

https://doi.org/10.1038/s43586-026-00511-5

Primer

Check for updates

Positron annihilation spectroscopy

Filip Tuomisto[1] ✉, Marie-France Barthe[2], Jakub Cizek[3], Stephan W. H. Eijt[4], Dermot G. Green[5], Gleb F. Gribakin[5], Christoph Hugenschmidt[6], Atsuo Kawasuso[7], Ilja Makkonen[1], Paweł Moskal[8], Farida Selim[9], Ewa Ł. Stępień[8], Alex Weiss[10] & Radoslaw Zaleski[11]

Abstract

Positrons are antiparticles of electrons that can serve as ultrasensitive probes of atomic-level structural detail in materials. When positrons annihilate with electrons, characteristic γ-rays are produced. Positron annihilation spectroscopy is based on the detection of the γ-photons emitted in the positron–electron annihilation process, and experimental methods analyse the time, energy and angular distributions of these γ-photons. In crystalline solids, the selective sensitivity of positrons to vacancy defects allows one to identify their structure and to determine their concentrations and physical properties in a wide range of materials. This Primer presents techniques in positron annihilation spectroscopy, evaluates the typical results obtained and highlights recent advances across various fields, ranging from point defects and porosity in solids to material surfaces and interfaces.

Sections

[1]Department of Physics and Helsinki Institute of Physics, University of Helsinki, Helsinki, Finland. [2]CEMHTI UPR3079, CNRS Orleans, University of Orleans, Orleans, France. [3]Faculty of Mathematics and Physics, Charles University, Prague, Czech Republic. [4]Department of Radiation Science and Technology, Delft University of Technology, Delft, The Netherlands. [5]School of Mathematics and Physics, Queen's University Belfast, Belfast, UK. [6]Heinz Maier Leibnitz Zentrum, Technical University of Munich, Garching, Germany. [7]National Institute for Quantum Science and Technology, Takasaki, Japan. [8]Faculty of Physics, Astronomy and Applied Computer Science, Jagiellonian University, Kraków, Poland. [9]Materials Science and Engineering, School for Engineering of Matter, Transport and Energy, Arizona State University, Tempe, AZ, USA. [10]Department of Physics, University of Texas at Arlington, Arlington, TX, USA. [11]Faculty of Physics, Maria Curie-Sklodowska University, Lublin, Poland. ✉e-mail: filip.tuomisto@helsinki.fi

Introduction

The positron is a fundamental particle — the antiparticle of the electron — with equal mass and opposite charge (where the charge, q, is equal to $+1e$, one elementary charge). The discovery of the positron coincided with the development of quantum mechanics, with seminal papers by P. A. M. Dirac, J. R. Oppenheimer and C. D. Anderson from the late 1920s and early 1930s[1–6] (Box 1). Although the positron is a stable particle, upon interaction with an electron, the two particles will annihilate each other and release electromagnetic radiation in the form of γ-photons with total energy, E, equivalent to $E \cong 2m_e c^2 \cong 1.022$ MeV (where m_e is the electron mass and c the speed of light in vacuum). Positron–electron annihilation was eagerly studied throughout the 1940s and 1950s, and several experimental methods were developed for this purpose[7–10].

The positron and electron can annihilate in a state where they are not bound to each other (called free positron annihilation) or, depending on their environment, can form a bound hydrogen-like state called positronium (Ps). *para*-Positronium (p-Ps) is a singlet spin state ($^1S_0$) with antiparallel electron and positron spins, whereas *ortho*-positronium (o-Ps) is a triplet ($^3S_1$) state with parallel electron and positron spins (Fig. 1a). p-Ps annihilates predominantly via the emission of two γ-photons of equal energy (511 keV each) at a rate of $\lambda = 8 \times 10^9 s^{-1}$ corresponding to a lifetime of $\tau = \lambda^{-1} = 125$ ps. o-Ps annihilation requires the emission of at least three γ-photons to conserve angular momentum and hence the annihilation rate is much slower corresponding to a lifetime of $\tau \cong 142$ ns. As a consequence, the dominant o-Ps annihilation channel in matter is a pick-off process where the positron annihilates with an electron from the surroundings, resulting in lifetimes in the nanoseconds to tens of nanoseconds regime. Ps can bind an additional electron to form a negative ion Ps^-, which annihilates with a lifetime $\tau = 500$ ps. The annihilation process of the free electron and positron is dependent on the structure of the positron–electron many-body system, and the corresponding lifetimes in solids are typically in the range $\tau = 100$–500 ps. Similarly to the self-annihilation of p-Ps, the free positron annihilation results in the emission of two γ-photons, each carrying the energy equivalent to the rest mass of one of the two particles (that is, 511 keV; Fig. 1b).

Low-energy positron interactions with atoms and molecules are characterized by strong correlations, including polarization of the molecular electron cloud, screening of the electron–positron Coulomb interaction and virtual-Ps formation (that is, back-and-forth tunnelling of an electron between the atomic ion and the positron). These interactions lead to binding of positrons to many atoms and molecules, enhancement of positron annihilation rates, and modification of the scattering properties and energy spectra of the annihilation photons. Energetic positrons entering gaseous, liquid or solid matter (or a plasma) rapidly lose their kinetic energy and eventually thermalize via collisions and electronic excitations, or through phonon emission

Box 1 | Historical developments in positron annihilation spectroscopy

1928: P. A. M. Dirac publishes *The Quantum Theory of the Electron* noting that the negative energy solutions are challenging to interpret[1].

1930: in a follow-up paper, Dirac suggests that the holes in the distribution of negative-energy electrons could represent protons[2].

1930: J. R. Oppenheimer publishes *On the Theory of Electrons and Protons* and concludes: "There are several grave difficulties which arise when one tries to maintain the suggestion that the protons are the gaps of negative energy, …"[3].

1931: in a subsequent paper, Dirac concludes: "A hole, if there were one, would be a new kind of particle, unknown to experimental physics, having the same mass and opposite charge to an electron. We may call such a particle an anti-electron."[4].

1932: C. D. Anderson publishes his unusual findings in cloud-chamber observations of cosmic rays: "For the interpretation of these effects it seems necessary to call upon a positively charged particle having a mass comparable with that of an electron…"[5].

1933: in a follow-up paper, Anderson names the newly found particle a positron: "It is concluded, therefore, that the magnitude of the charge of the positive electron which we shall henceforth contract to positron is very probably equal to that of a free negative electron which from symmetry considerations would naturally then be called a negatron."[6].

1934: theory suggests the existence of a bound positron–electron state[260].

1942: the first angular correlation experiments of annihilation quanta are published[7].

1945: the bound positron–electron state is named positronium[261].

1946: the theory of positron–electron bound states is extended to polyelectrons, known as Ps^- and Ps^+ three-particle bound states[262].

1949: the theory of positrons leads to the development of quantum electrodynamics[263].

1949: the first measurement of deviation from collinear angular distribution of annihilation quanta is published[8].

1949: the first positron lifetime measurement is published[9].

1951: experiments prove the existence of positronium through three-quantum decay, which leads to the discovery of strong positron attachment to certain polyatomic molecules[208,264].

1953: positron emission tomography is developed and the first clinical positron image of a patient with a recurring brain tumour is published[220].

1957: the results of the first spin-resolved positron annihilation experiment are published[10].

1958: S. Berko and J. S. Blaskett give a theoretical description of the wavefunction of a delocalized positron in a crystal lattice[265].

1967: positron trapping at defects is discovered in experiments[90].

1968: the first measurements of Doppler broadening of positron–electron annihilation radiation are published[266].

1970: C. H. Hodges gives a theoretical description of positron trapping and the trapped state in a solid[267].

1976: the first coincidence Doppler broadening measurements are published[268].

1988: the first measurements of positron-induced Auger electrons are published[29].

1990s and beyond: expansion of the use of positron annihilation spectroscopy with widespread foundational developments of experimental methods and instrumentation, theoretical models and computational approaches.

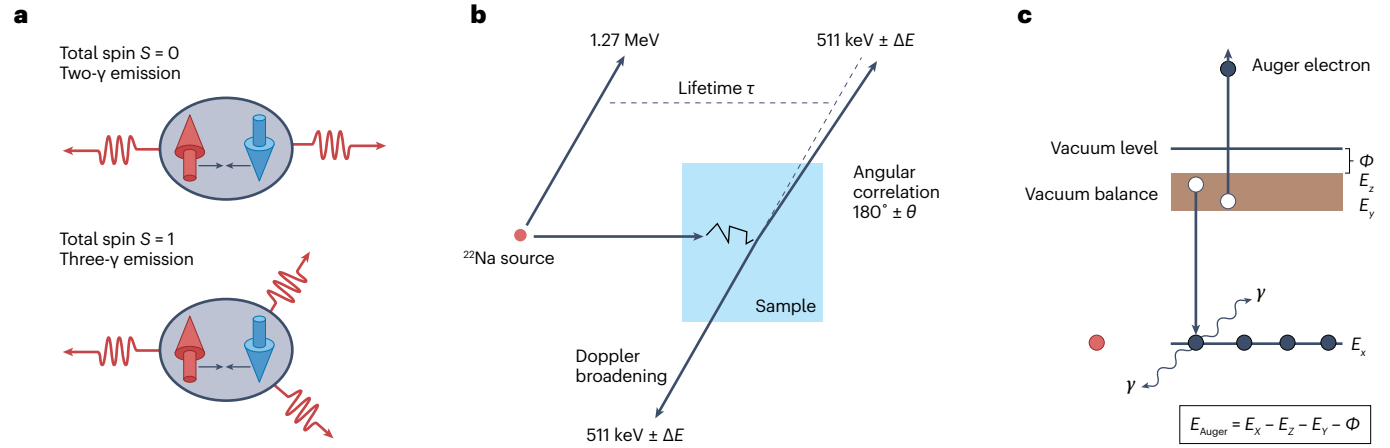

Fig. 1 | Overview of positron annihilation processes. a, A schematic representation of *para*-positronium (p-Ps) with total spin $S = 0$, *ortho*-positronium (o-Ps) with total spin $S = 1$, and associated γ-ray emission in the annihilation process. **b**, A schematic of free positron annihilation in a sample with associated measurables including positron lifetime, Doppler broadening and angular correlation, where E is the total energy. **c**, A schematic of positron annihilation-induced Auger emission where γ is the annihilation γ-photon, E_{Auger} is the energy of the Auger electrons, E_x, E_y and E_z are the energy levels of the electrons participating in the Auger process, and φ is the electron work function. τ, positron lifetime.

in solids. The thermalized positrons easily form Ps with the electrons if the surrounding system contains a large concentration of voids, such as molecular and porous matter, making p-Ps and o-Ps annihilation important in these cases. In the periodic lattice of a perfect crystalline solid, the ground state of a thermalized positron is a Bloch-like state delocalized in the interstitial space owing to strong Coulombic repulsion between the positron and the atomic nuclei. Most experiments are set up in a way that at any given time only a single positron interacts with matter. Interruptions in the periodicity (such as defects) can lead to the localization of the positron, and in particular vacant lattice sites are efficient traps with typical binding energy of the order of 1 eV. The positron state as well as the atomic and electronic structures determine the annihilation rate, the energy and the angular spectra of the annihilation radiation, making them key spectroscopic signals. The annihilation process corresponds to the annihilation of a free positron and electron, but the characteristics are strongly modified by the environment. At the surface of a solid (such as the solid–vacuum interface), the positron may be re-emitted to the vacuum, trapped in a surface state or form Ps.

The purpose of this article is to introduce the set of methods collectively called positron annihilation spectroscopy (PAS)[11,12], with a focus on applications in crystalline solids[13–21]. The experimental methods are based on detecting the γ-photons emitted in the positron–electron annihilation process, and analysing their time, energy and angular distributions. Importantly, the positron state in a solid and the positron–electron annihilation characteristics can be also modelled with first principles approaches, and the results can be compared with experimental data. An accurate theoretical description of the positron–matter system is, however, a challenging many-body problem, and theory has typically lagged behind experiments. The selective sensitivity of positron-related methods to vacancy defects allows for determination of vacancy structure and concentrations within a wide range (10 ppb to 100 ppm). As a general rule, positron trapping at vacancy defects leads to a reduced overall annihilation rate (increased lifetime) and a narrower energy and angular distribution of annihilation radiation. PAS can be applied to bulk samples as well as thin films, and there are no restrictions on the physical characteristics such as electrical conductivity or optical properties of the studied material. In semiconductors, the sensitivity to the charge states of the defects allows one to combine functional and structural information. Positron annihilation can also be used to monitor atomic-scale structures on surfaces, in nanostructured and porous systems, and in biomatter[22,23]. Although polymers and liquids can be studied with PAS[23], this Primer focuses on its application to solids. In this Primer, we give an overview of the various PAS techniques. We start with examples of applications in crystalline semiconductors, metals and ceramics, discussing radiation damage and spin-related phenomena. We continue with materials with more complex atomic structures, such as hybrid perovskites and metal–organic frameworks. We also discuss positron annihilation-based methods applied to surface phenomena (positron annihilation-induced Auger-electron spectroscopy; Fig. 1c) and to medical imaging (positron emission tomography). Finally, we give a brief overview of the anticipated future developments in PAS.

Experimentation

This section provides a brief overview of the experimental set-ups using positrons either from isotope sources or produced at large-scale facilities. Safety considerations and sample preparation are also discussed. The main measured quantities include positron lifetime, Doppler broadening and angular correlation of the annihilation radiation, and positron annihilation-induced Auger electrons are described.

Facilities

Table top. Positrons can be generated by using radioisotopes that undergo β^+ decay. In these radioisotopes, the emitted positrons exhibit a continuous energy spectrum owing to the distribution of energy between the positron and the co-emitted neutrino, typically ranging in mean energy up to hundreds of kiloelectronvolts. In some radioisotopes, the daughter nucleus is left in an excited state and emits a de-excitation γ-ray, known as the 'start photon', almost simultaneously with the positron. The most commonly used β^+ radioisotope for positron annihilation experiments is ^{22}Na, which has a half-life of 2.6 years and decays into ^{22}Ne* that subsequently decays into ^{22}Ne in

only ≈3.7 ps by emitting a 1,274-keV γ-ray. To create a positron source, a small amount of β^+ radioisotope (≈1 MBq activity) is sealed between two thin (a few micrometres) metal or polymer foils[24]. This source is placed between two sample pieces during measurements, allowing emitted positrons to penetrate the sample up to 1 mm depth, with the extent of the exponential stopping profile depending on the mass density of the material (Fig. 2a). A small fraction of positrons annihilate within the source and covering foil, which is known as the 'source contribution' and must be accounted for in data analysis[25].

Isotope-based beams. For studying near-surface phenomena in materials, the positrons emitted by a radioisotope can be moderated by using solid noble gases (such as neon) or heavy metal elements (such as tungsten) that have a negative work function for positrons[15,22]. In these slow positron beams (also known as variable-energy positron beams), the mono-energetic positrons emitted by the moderator are re-accelerated to energies in a typical range of 0.1–50 keV and electromagnetically or electrostatically guided to the studied sample. This allows tuning the positron implantation depth from nanometres to micrometres (Fig. 2b). As the moderation process has relatively poor efficiency, the radioisotope activity required in such beams is typically of the order of 1 GBq. The time information carried by the 'start photon' is lost owing to the low moderation efficiency, but timing can be re-introduced, for example, through electromagnetic chopping and bunching of the otherwise continuous beam.

High-intensity sources. High-intensity positron beams are generated by pair production using intense γ sources at large-scale facilities, such as linear accelerators (using bremsstrahlung) or nuclear reactors (with nuclear γ radiation). Efficient positron–electron pair creation requires high γ energy, typically in the range of 1–35 MeV (refs. 26,27) as the pair production cross section increases roughly with ln(E) and scales as Z^2 (square of the atomic number of the target). Therefore, dense high-Z materials such as tantalum, tungsten or platinum are preferred as converters. At the NEutron induced POsitron source MUniCh (NEPOMUC), after thermal neutron capture in cadmium, high-energy prompt γ rays are converted into positron–electron pairs in platinum, which serves to moderate the emitted positrons[28]. Tungsten is used at the ELBE electron linac-based MePS and GiPS high-intensity positron beams and at the TU Delft Reactor Institute POSH-beam to convert high-energy γ-rays into electron–positron pairs and subsequently moderated emitted positrons[26,27].

Safety considerations. Dealing with radioisotopes such as ^{22}Na, as well as operating high-intensity sources at nuclear reactor or accelerator facilities, requires radiation protection measures adapted to each situation. For example, in table-top experiments, the source activity is typically very close to or even below the exemption limit (1 MBq for ^{22}Na) and hence the required radiation protection measures are relatively modest. Handling of radioactive sources nevertheless must follow the detailed radiation protection regulations of each country where the experiments are performed. Isotope-based beams that use radioactive sources of 1,000-fold activity require shielding — usually a 'castle' constructed of lead bricks — at the source end of the beam. However, these sources are handled only every 5–10 years when replacing the source. At the sample end, the positron flux and the emission

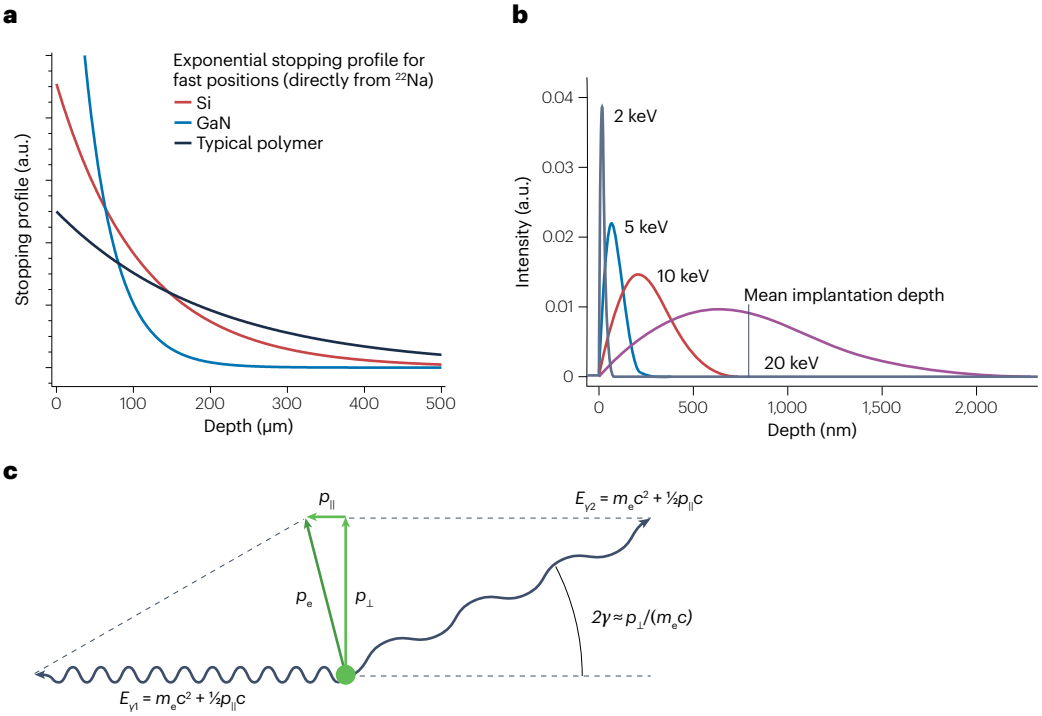

Fig. 2 | Positron and electron kinetic energies. a, The exponential stopping profile of positrons emitted by a ^{22}Na source in materials with different mass densities. **b**, Implantation profiles of mono-energetic positrons implanted at different energies into a material with ~6 g cm^{-3} mass density. **c**, A schematic of the electron-momentum-dominated Doppler effect and angular deviation in the two-γ annihilation process. The momentum (p_e) of the centre of mass of the annihilating positron–electron pair causes a Doppler shift in the γ-energies ($E_{\gamma1,2}$) through its component parallel to the measurement direction ($p_{||}$). The perpendicular component of the momentum ($p_\perp$) is responsible for the angular deviation. a.u., arbitrary units; c, speed of light; m_e, electron mass.

of annihilation-induced γ rays is low and does not require shielding. With high-intensity sources, safety measures depend on the type of the host facility.

Sample preparation

A key benefit of positron annihilation methods is that a positron injected to a material — solid, liquid or even gaseous — will eventually annihilate with an electron and produce a measurable signal. For solid samples measured with table-top set-ups, typically two sample pieces each with a minimum 5–10-mm diameter (exact shape does not matter) and a flat surface are required for making the sample–source–sample 'sandwich'. The thickness of the sample depends on the mass density of the material and needs to be sufficient enough to stop all the positrons emitted by the sample. Samples are typically 0.5 mm or thicker. Although there is no theoretical maximum to the allowed sample thickness, in set-ups with temperature control the size of the vacuum chamber surrounding the sample is often minimized, setting a practical limit of typically 1–2 mm. The flatness of the surface facing the source is important only from a mechanical perspective to avoid any air pockets between the source and the sample, hence an optically flat surface is usually sufficient. There are no restrictions on the electrical, optical, magnetic, thermal or mechanical characteristics of the samples. When using variable-energy beams for studying near-surface or surface phenomena in thin films, for example, the quality of the surface is more important than in table-top set-ups. A minimum film thickness of a few hundred nanometres is often required to avoid issues caused by diffusion of thermalized positrons to the surface or the film–substrate interface. In specific cases where the positron diffusion length is strongly reduced, much thinner films, down to a few nanometres, can be studied.

Measured quantities

Lifetime. The time between the positron implantation into the sample and its annihilation determines the lifetime of the individual positron (Fig. 2c). This lifetime can be experimentally determined by measuring the time difference between the start γ-ray (indicating positron emission) and one or both of the annihilation γ-rays (indicating positron annihilation) with fast scintillation detectors. Positron annihilation is a stochastic process. If there is only a single positron state in the sample, the probability, $n(t)$, that a positron is still alive at a certain time, t (measured from its implantation time), decays exponentially over time, as described by the equation $n(t) = n_0 e^{-t/\tau}$, where τ is the decay parameter known as the positron lifetime — the reciprocal of the annihilation rate, λ — and n_0 is the probability at $t = 0$. The measured time differences between the start and annihilation signals will follow $\frac{\mathrm{d}}{\mathrm{d}t}(1 - n(t)) = -\frac{\mathrm{d}}{\mathrm{d}t}n(t)$. In cases where positrons can occupy multiple states within the samples — such as delocalized positrons and those trapped at various defects — there will be multiple exponential components, each characterized by a unique decay parameter representing the positron lifetime in the corresponding state.

Doppler broadening and angular correlation of annihilation radiation. The non-zero centre-of-mass momentum of the annihilating positron–electron pair leads — through momentum conservation — to a slight deviation from the 180° angle between the two emitted 511 keV annihilation γ-rays. This deviation is given by the angle $\theta \simeq p_\perp/(m_0 c)$, where $p_\perp$ is the component of the centre-of-mass momentum perpendicular to the direction set by one of the emitted γ-rays, and m_0 and c are the electron (positron) mass and speed of light, respectively. In practice, these deviations extend up to 100 mrad (about 6°) and can be measured with position-sensitive detectors (such as a scintillator array) in one or two dimensions through a technique known as angular correlation of annihilation radiation (ACAR and 2D-ACAR, respectively)[13]. Similarly, owing to the Doppler effect, there is a slight deviation of the annihilation γ-ray energies from 511 keV given by $\Delta E = \pm p_\parallel c/2$, where $p_\parallel$ is the component of the centre-of-mass momentum along the direction of the emitted γ-rays. The electron-momentum distribution results in Doppler broadening of the 511 keV annihilation line that can be measured by high-purity germanium detectors that offer sufficient energy resolution. Measurable Doppler broadening extends up to about ±15 keV. The Doppler broadening values are typically expressed in momentum units of 10^{-3} $m_0 c$ that corresponds to 1 mrad in ACAR experiments, or in atomic units (1 keV ~ 0.54 a.u. ~ $3.9 \times 10^{-3} m_0 c$ ~ 3.9 mrad).

Positron annihilation-induced Auger electrons. Positron annihilation-induced Auger electron spectroscopy (PAES) is an advanced surface-sensitive technique in which low-energy positrons annihilate with core-level electrons in the outermost atomic layer of a material. It produces Auger electrons (Fig. 1c) without the high secondary-electron background inherent to conventional electron-induced Auger spectroscopy, in which core electrons are removed by photo-ionization or electron-impact ionization. This results in spectra without secondary electron background at higher Auger energies[29,30]. Furthermore, the Auger-electron emission is decoupled from the positron impact position, so the probed atoms remain unperturbed by the primary particle. The main limitation of PAES is the need of high positron beam intensity to compensate for inherently long measurement times[31]. Data analysis follows the principles of Auger electron spectroscopy.

Results

This section gives a brief overview of the data analysis associated with positron lifetime and Doppler broadening experiments. The basics of ab initio theoretical calculations that are used to predict the annihilation parameters associated with various positron states are also described. For in-depth treatments, we refer the reader to refs. 17,18.

Data analysis

Lifetime. To gather sufficient statistics of positron annihilation events, millions of occurrences are measured. The resulting histogram (Fig. 3a) is known as the positron lifetime spectrum (the experimental method is sometimes referred to as positron annihilation lifetime spectroscopy, or PALS) and consists of a sum of exponential components, $\sum_i I_i e^{-t/\tau_i}$, convoluted with the resolution function of the spectrometer that can be fitted to the experimental data, and includes a constant background from random coincidences. From the lifetimes, τ_i, and relative intensities, I_i, of the resolved components, the trapping rates of positrons at the defects in the sample can be estimated using an appropriate trapping model (set of rate equations) that describes the kinetics of positron trapping in the sample. The defect concentrations (or densities) are obtained from these trapping rates through trapping coefficients that represent the cross-sections for positron trapping per unit concentration of defects. For an in-depth description of positron trapping and associated models, we direct the reader to refs. 17,18. The order of magnitude of the positron trapping coefficient for various types of defects (such as vacancies, dislocations and vacancy clusters) is generally similar across different materials, allowing to make reasonable

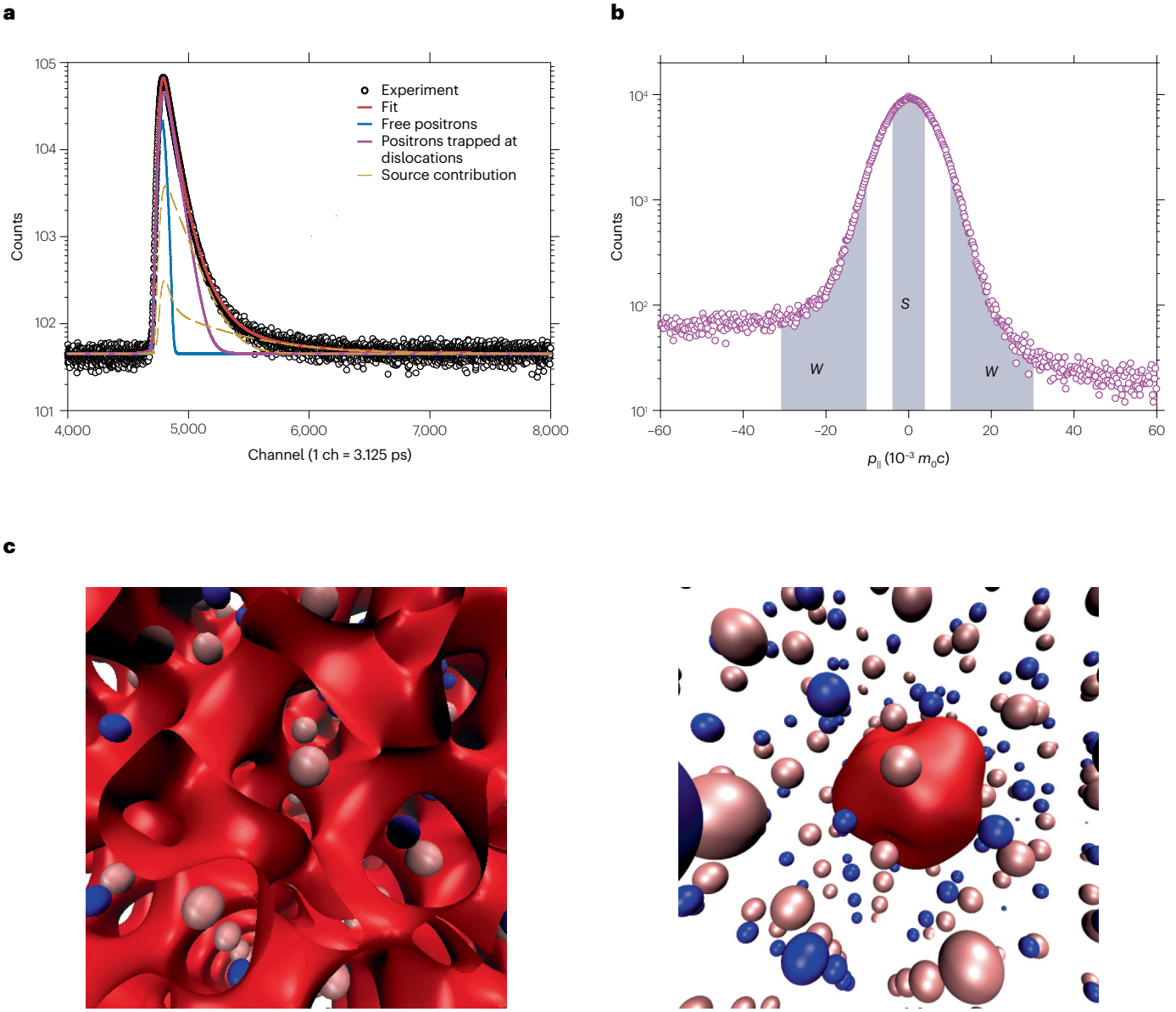

Fig. 3 | Positron lifetime, Doppler broadening and the positron state in a lattice. a, An example of a measured positron lifetime spectrum with three fitted components shown, interpreted to originate from the annihilations of free positrons, trapped positrons and the source. **b**, An example of a measured Doppler broadening spectrum showing the definition areas of the integrated *S* and *W* parameters. $p_{||}$ is the component of the centre-of-mass momentum along the direction of the emitted γ-rays. m_0 and *c* are the electron (positron) mass and speed of light, respectively. **c**, The positron density isosurface (red) of a delocalized positron in the crystal lattice of GaN (left) and of a trapped positron in a gallium vacancy defect in GaN (right) obtained by ab initio theoretical calculations. Blue and pink balls represent gallium and nitrogen atoms, respectively. ch, channel. Part **a** adapted with permission from ref. 19, Elsevier.

concentration estimates even in cases where the positron trapping coefficient has not been determined accurately.

An important parameter is the average positron lifetime, $\tau_{ave} = \sum_i I_i\tau_i$, that coincides with the centre of mass of the annihilation spectrum, as it can be determined with very high accuracy even when resolving the lifetime components is challenging. An elevated τ_{ave} means that positrons annihilate as trapped at open volume defects. Positron lifetimes exceeding ~1 ns indicate the formation of Ps and the presence of large (0.5–50-nm diameter) free volumes.

Doppler broadening and ACAR. The typical energy resolution of a high-purity germanium detector is relatively broad compared with the full width of the Doppler-broadened peak (the experimental method is sometimes referred to DBS for Doppler broadening spectroscopy), and the peak-to-background ratio in a conventional experiment with a single detector is rather low, only about 10^2. Integrated shape parameters, *S* and *W*, represent fractions of counts in various areas under the Doppler broadened peak and are used to characterize the 511-keV annihilation line (Fig. 3b). The *S* parameter is defined as the ratio of the

counts in the central region of the annihilation line to the total number of the counts in the line and represents annihilations of positrons with low-momentum electrons. The *W* parameter is the fraction of the counts in the wing regions of the line. Valence electrons mostly contribute to the *S* parameter, owing to their diffuse spatial extent and thus a correspondingly relatively narrow momentum distribution, whereas only core electrons have momentum values high enough to contribute to the *W* parameter. *S* and *W* are sometimes called the valence and core annihilation parameters, respectively. The *S* parameter can be described as carrying information about the (excess) open volume, while the *W* parameter carries information on the chemical identities of atoms surrounding the annihilation site. It is important to know that the absolute values of the *S* and *W* parameters do not have a physical meaning, they only describe the shape of the 511-keV peak. Examples of analysing *S* and *W* parameters are provided in the 'Applications' section.

The resolution and peak-to-background ratio of the Doppler broadening measurement can be improved by measuring the annihilation radiation with two (collinear) detectors and imposing coincidence conditions in an experiment called coincidence Doppler broadening (CDB). The shapes of the annihilation lines obtained in this way can be analysed in more detail, typically in the form of 'ratio curves', in which the annihilation line of interest is point-by-point normalized by a reference spectrum[18,32]. ACAR experiments exhibit inherently narrower resolution than Doppler broadening experiments (including CDB) and can be analysed with similar 'ratio curve' approaches, including comparison to ab initio calculations[33]. The 2D-ACAR experiments provide mapping of the symmetry of the electronic structure with high resolution, a property that is particularly useful for studying fermiology. When studying defects, Doppler experiments are more common owing to their shorter measurement times and simpler instrumentation. In atomic and molecular gases, time-dependent measurements of Doppler broadening, known as age-momentum correlation spectra, can probe positron temperature and cooling dynamics[34].

Theoretical calculations

Theoretical calculations can be used for experimental interpretation and design, as well as to understand fundamental processes[18]. For example, measured lifetime components and Doppler lineshapes can be connected to the microscopic structures of defects and defect complexes that trap positrons. The accurate theoretical description requires proper treatment, or at least approximation, of the positron–electron many-body correlations. For solid-state matter and defects, the standard affordable method is the two-component electron–positron density functional theory (DFT)[35], in which the fundamental variables include the total energy, *E*, and the average electron and positron densities, $n_-(\mathbf{r})$ and $n_+(\mathbf{r})$, respectively. Figure 3c shows an example of the calculated positron density in a defect-free lattice (here, a fully delocalized positron in GaN) and of a positron trapped at a vacancy defect (here, a gallium vacancy in GaN). The solutions of the positron and electron densities and wavefunctions are used to extract the annihilation rates and momentum densities (such as Doppler broadening and ACAR) as described below. In addition to the electron–electron exchange and correlation energy functional of the traditional one-component DFT, one has to parametrize an electron–positron correlation energy functional and an enhancement factor that describes the increase in the annihilation rate owing to the screening of the positron by electrons.

Most practical calculations are done in the limit of zero positron density, and the electronic structure and density are solved first without the effect of the positron[18]. Standard electronic structure methods such as plane-wave pseudopotential codes can be used for this. The potential of the positron is solved with the Schrödinger-like equation

$$V_+(\mathbf{r}) = -\int \mathrm{d}\mathbf{r}' \frac{n_{\mathbf{r}'}}{|\mathbf{r}-\mathbf{r}'|} - V_{\mathrm{ext}}(\mathbf{r}) + V_{\mathrm{corr}}(\mathbf{r}) \quad (1)$$

where $\mathbf{r}$ is the position, $\mathbf{r}'$ is the source position and $n_-(\mathbf{r}')$ is the average electron density. The first term describes the average electrostatic potential from electrons, V_{ext} describes the external potential of the nuclei, and V_{corr} is the electron–positron correlation potential. The annihilation rate, λ, is approximated by

$$\lambda = \frac{1}{\tau} = \pi r_e^2 c \int d\mathbf{r} n_+(\mathbf{r}) n_-(\mathbf{r}) \gamma(n_-(\mathbf{r})), \quad (2)$$

where τ is the positron lifetime, r_e is the classical radius of the electron, c is the speed of light and $\gamma(n_-(\mathbf{r}))$ is the parametrized enhancement factor. The $\gamma(n_-(\mathbf{r}))$ is the most crucial approximation in DFT-based lifetime calculations and the choice of the model used for its parametrization essentially determines the lifetime. The momentum density of annihilating pairs measured in Doppler broadening spectroscopy cannot be formulated exactly in DFT. The models include various kinds of enhancement factors[18] as well as density functionals that may involve dependence on position (and hence momentum) or electron states. The following probability sums over occupied electron states, j

$$\rho(\mathbf{p}) = \pi r_e^2 c \sum_j \left| \int d\mathbf{r} \exp(-i\mathbf{p}\cdot\mathbf{r}) \psi_+(\mathbf{r}) \psi_j(\mathbf{r}) g_j(\mathbf{r}) \right|^2, \quad (3)$$

where $\mathbf{p}$ is momentum, ψ_+ is the positron wavefunction, ψ_j is the electron wavefunction corresponding to state j, and g_j is the state-dependent enhancement factor. Before comparing the theoretical result with experiments, the three-dimensional momentum density of annihilating pairs, $\rho(\mathbf{p})$, is projected on the longitudinal direction (p_L) of the Doppler experiment

$$\rho(p_L) = \int dp_x \int dp_y \rho(\mathbf{p}) \quad (4)$$

and convoluted with the experimental resolution function, which is typically a Gaussian function with a full width at half maximum on the order of 1 keV. Other many-body theory-based approaches including quantum Monte Carlo and diagrammatic many-body theory offer a route to fully ab initio calculation of momentum distributions and annihilation rates without any reliance on approximations from electron gas.

Applications

This section presents applications of PAS using different modalities in a variety of materials. Examples in semiconductors, metals and ceramics, as well as radiation damage, cover the use of positron lifetime and Doppler broadening approaches in crystalline solids. Spin-polarized beams are used to study magnetic phenomena. The hybrid organic–inorganic character of solar cell perovskites results in large differences in the sizes of vacancy defects as well as in the associated positron lifetimes. In materials with larger open volume structures such as metal–organic frameworks positronium formation and long lifetimes are important. Positron annihilation-induced Auger electron emission can also be used to study surface phenomena.

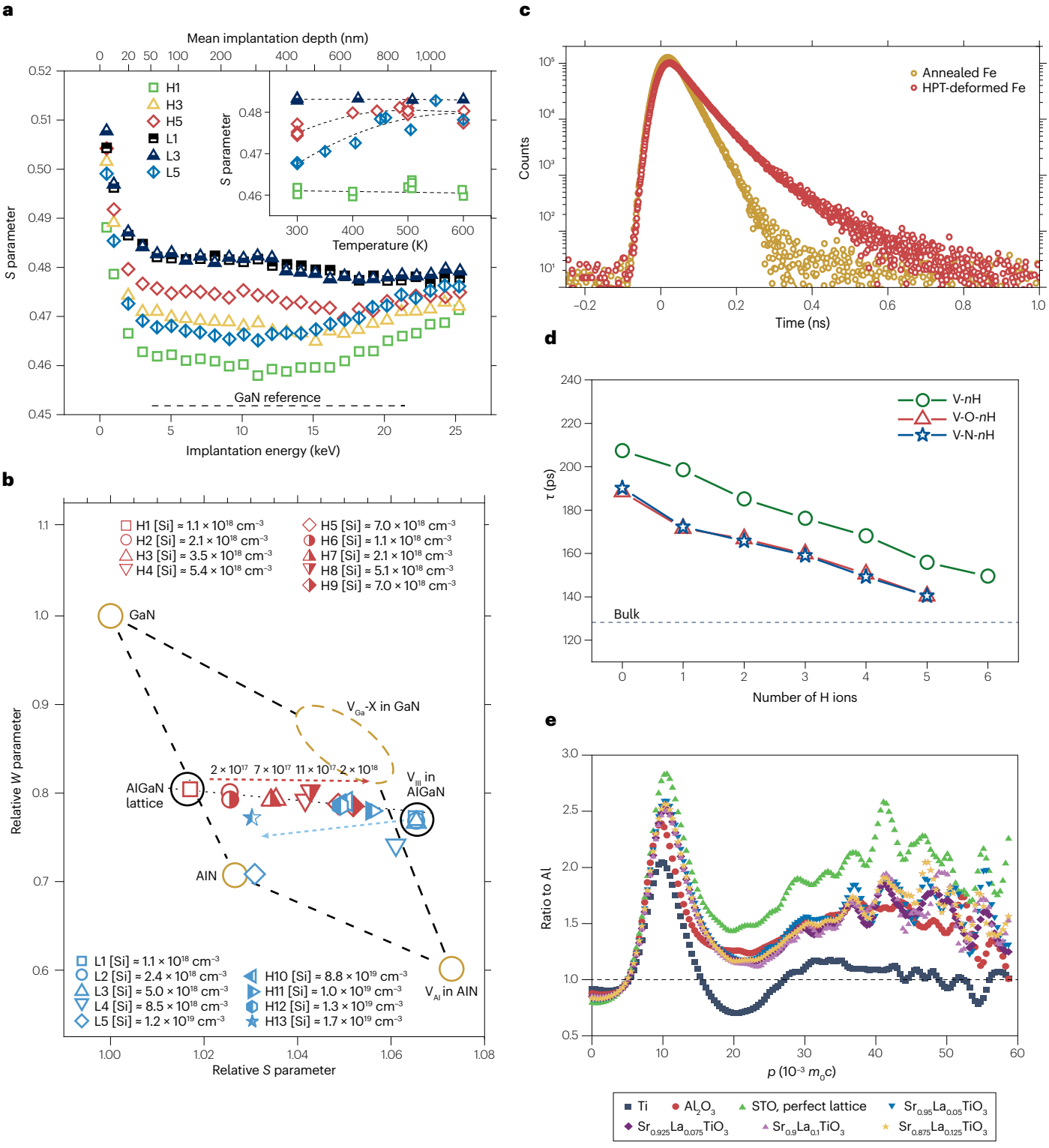

Semiconductors

Positron trapping at defects in semiconductors is charge-state sensitive owing to the lack of efficient screening of Coulomb attraction and repulsion. The trapping coefficient for negatively charged vacancies is proportional to $T^{-1/2}$, where T is the sample temperature. At room temperature, the trapping coefficient for negatively charged vacancies is approximately twice that for neutral vacancy defects. Positrons can also get trapped in Rydberg states of negatively charged defects, even if they do not have any open volume, such as acceptor impurities. However, the low binding energy (typically, 30–100 meV) of these shallow states leads

Fig. 4 | Examples of positron lifetime and Doppler broadening data in semiconductors, metals and ceramics. a, The *S* parameter for selected AlGaN samples (H with high carbon content, L with low carbon content) as a function of positron implantation energy. The inset shows the temperature dependence of the *S* parameter measured at around 7 keV. **b**, A (*S*, *W*) plot of relative parameters, referenced to GaN, in a large set of Si-doped AlGaN samples. V indicates the vacancy type. **c**, Example positron lifetime spectra for iron annealed at 900 °C for 1 h in a vacuum and iron subjected to severe plastic deformation using high-pressure torsion (HPT). The curves show the fitted sum of exponential decay components convoluted with the resolution function of the spectrometer **d**, The calculated positron lifetimes, τ, for the bulk (shown with the dashed line), vacancy complexes (V) with hydrogen (H), oxygen (O) and nitrogen (N) impurities in niobium. **e**, Coincidence Doppler broadening ratio curves (normalized to pure aluminium) for $SrTiO_3$ and $Sr_{1-x}La_xTiO_3$ ceramics and for pure Ti and Al_2O_3, where *x* is the stoichiometric amount. Part **a** adapted with permission from ref. 46, AIP. Part **b** adapted from ref. 49, CC BY 4.0. Part **d** adapted from ref. 259, CC BY 4.0. Part **e** adapted with permission from ref. 84, Elsevier.

to efficient escape of the trapped positrons at elevated temperatures. Therefore, these negative ion-like defects are efficient positron traps below room temperature. As the Bohr radius of such a state is large compared with the inter-atomic distance in the lattice, a positron trapped at a negative ion will exhibit identical annihilation characteristics with the delocalized state in the lattice. As the defect charge states can be manipulated by illumination of the samples[36,37], or by applying an electrical bias during experiments, the functional character of the defects can be analysed simultaneously with their structural identification.

Positron annihilation has been used with great success to make contributions to the understanding of vacancy defects in a wide variety of semiconductors[16–18,21]. For example, the family of III-nitride binary compound semiconductors GaN, AlN and InN has been studied extensively. PAS has identified that the main native acceptor defect in n-type GaN and InN is the metal vacancy[38,39]. However, in AlN, positron experiments have shown that it is not the aluminium vacancy[40] but might be the nitrogen vacancy[41]. PAS can also be used for the identification and monitoring of defects created in ion implantation processing of GaN with magnesium as well as the subsequent ultrahigh-pressure-annealing for obtaining p-type material[37,42–44].

Recently, PAS has been increasingly used to study (In,Ga)N, (In,Al)N and (Al,Ga)N alloys as well as opto-electronic and power electronic devices of these materials[45–49]. In particular, the compensation of n-type doping is an unresolved issue in ultrawide bandgap high-aluminium (Al,Ga)N alloys. Figure 4a shows Doppler broadening data measured in thin-film $Al_{0.90}Ga_{0.10}N$ samples (labelled H1, H3, H5, L1, L3 and L5) doped to various degrees with Si[49], where the S parameter is monitored as a function of positron implantation energy and the corresponding mean implantation depth in selected samples measured at room temperature. In the sample labels, H stands for high carbon content and L for low carbon content, corresponding to carbon concentrations of 2×10^{18} cm^{-3} and 2×10^{17} cm^{-3}, respectively, with silicon concentration ranging from 1×10^{18} cm^{-3} to 1.2×10^{19} cm^{-3}. The *S* parameter depth profiles can be analysed by comparing with solutions of the stationary positron diffusion equation and corresponding best-fit analysis[50]. The *S* parameter measured in a GaN reference sample where positrons only annihilate in the free state in the lattice is marked with a dashed line. For the alloy samples, the *S* parameter decreases from its initial surface value at low energies of 0–4 keV with increasing energy to the value of the 600–800-nm-thick (Al,Ga)N layers, where it is almost constant in the range of 6–15 keV. At energies above 15 keV, the *S* parameter gradually approaches the values characterizing the substrate. The inset shows the effect of measurement temperature on the *S* parameter characterizing the (Al,Ga)N layers (6–15-keV implantation energy range), demonstrating the effect of ionized carbon acceptor shallow traps unintentionally present in the samples.

Figure 4b shows the layer-specific *S* and *W* parameters measured in a large set of Si-doped $Al_{0.90}Ga_{0.10}N$ samples as (*S*, *W*) data. The parameters are shown as normalized to those measured in the GaN reference sample and called relative parameters. The green markers connected by the dashed lines denote parameters determined in earlier studies for 'defect-free' AlN as well as the parameters characteristic of in-grown V_{Ga} defects (V_{Ga}–X) in GaN and V_{Al} in AlN. V_{Ga} denotes vacancy defects on the Ga sublattice of the GaN compound, while V_{Ga}–X is a complex of V_{Ga} and an unknown defect that can be intrinsic or extrinsic. For example, V_{Ga}–O_N would constitute of V_{Ga} and an oxygen impurity substituting for an adjacent nitrogen atom. The plot indicates that in the case of an AlN sample where all positrons would annihilate as trapped at V_{Al}, the experimental *S* and *W* parameters will be found at the 'V_{Al} in AlN' point. If the experimental data are found on the line connecting the 'AlN' and 'V_{Al} in AlN' points, the sample contains V_{Al} defects at a concentration determined by the position on the line. In the absence of other defects, half-way between the two end points corresponds to low–10^{17} cm^{-3} in vacancy concentration. In the case of the $Al_{0.90}Ga_{0.10}N$ samples in question, all the measured (*S*, *W*) data fall inside the area defined by the above-mentioned four points, as expected for an alloy. The data form a straight line, indicating that these samples contain two (and only two) distinct states in which the positrons annihilate. At the left end, the (*S*, *W*) data fall close to the line connecting GaN and AlN lattice values and represent the 'defect-free' AlGaN alloy. At the right end of the line, with increasing silicon concentration, the data points converge at the line connecting V_{Ga}–X in GaN and V_{Al} in AlN. The trend-like shift of the (*S*, *W*) parameters shown with red markers towards the vacancy-like data in these samples indicates an increase in the cation vacancy concentration with increasing silicon doping. Further increase in the silicon content, as shown by the behaviour of the (*S*, *W*) data with blue markers, results in a very different behaviour, with the data shifting strongly to AlN-like values, possibly related to Si–DX centre formation[49]. These data demonstrate the sensitivity of the positron annihilation parameters to the atomic identities of the surroundings, in particular, the (*S*, *W*) parameters of the vacancy defects found in these samples are found in regions with more gallium in their surroundings than on average in the lattice. On the other hand, the Si–DX behaviour exhibits almost purely AlN-like values, strongly suggesting that these centres have no Ga atoms in the immediate vicinity.

Metals and alloys

Vacancies in metals are always electrically neutral owing to the screening effect of conductive electrons making positron annihilation studies of vacancies in metals simpler as compared with those in semiconductors. PAS provides an accurate determination of the concentration of thermal vacancies in metals[51–55]. By analysing the thermodynamically equilibrium concentration of vacancies as a function of temperature using an Arrhenius plot, one can accurately determine the vacancy formation enthalpy[51,52,55].

The concentration of non-equilibrium vacancies, introduced by processes such as quenching from high temperatures[56,57], irradiation with energetic particles[58–61] or plastic deformation[62,63], can also be determined using PAS. The lifetime of a trapped positron increases with the open volume of the defect. Therefore, positron lifetime measurements can distinguish between monovacancies and vacancy clusters formed by agglomeration of multiple vacancies as can be seen through the much longer lifetime in high-pressure torsion deformed Fe compared with annealed Fe (Fig. 4c). The lifetimes of positrons trapped in vacancy clusters with various numbers of vacancies can also be calculated[64,65]. By comparing experimental positron lifetimes with the calculated curves, the average size of vacancy clusters in the sample can be determined[63]. Furthermore, studying the development of vacancies with temperature and their agglomeration into vacancy clusters allows one to determine the vacancy migration energy[53,59].

Vacancies in metals can form complexes with certain impurities when binding to vacancies is energetically favourable. The presence of such impurities in metals reduces the vacancy formation enthalpy and facilitates the creation of vacancies. A prominent example of this phenomenon is hydrogen absorbed in the metal lattice, which greatly lowers the vacancy formation enthalpy and causes a substantial increase in the equilibrium concentration of vacancies[66,67]. The presence of hydrogen bound to a vacancy shortens the lifetime of the trapped positron owing to the repulsive interaction between the positron and hydrogen, which reduces the localization of the positron in the vacancy[68]. Accurate measurement of the positron lifetime, along with a comparison of experimental data with ab initio modelling of vacancy–hydrogen complexes, allows one to determine the number of hydrogen atoms attached to a vacancy (Fig. 4d). For instance, in niobium, vacancies can trap up to four hydrogen atoms[60,68].

Impurities or solute atoms bound to vacancies not only influence the concentration of vacancies but also suppress the mobility of vacancies. Consequently, diffusion-limited processes, such as solute clustering and precipitation, can be inhibited by microalloying elements that bind to vacancies and suppress their mobility[69]. This phenomenon can be used, for example, to suppress natural ageing in aluminium alloys[70]. The chemical nature of solutes bound to vacancies can be determined using coincidence Doppler broadening spectroscopy[71], which provides information about the local chemical environment of positron annihilation sites.

Alloys can contain various types of vacancies, depending on which alloying element is missing. Vacancies located in crystallographically non-equivalent lattice sites are generally characterized by different positron lifetimes. However, the differences in positron lifetimes may be too small to distinguish between different types of vacancies, particularly when the alloying elements have similar atomic radii. Nevertheless, the local chemical environments of various types of vacancies often differ greatly, allowing one to distinguish between them combining positron lifetime measurements with coincidence Doppler broadening[72]. For example, in the Fe_3Al intermetallic compound, vacancies are almost exclusively located in the iron sublattice. The lifetimes of positrons trapped in iron and aluminium vacancies are quite similar, but the local chemical environments of the two types of vacancies are very different. Iron vacancies are directly surrounded only by aluminium, whereas aluminium vacancies are surrounded exclusively by iron. This difference in the chemical environment allows both types of vacancies to be distinguished by combining lifetime measurements with coincidence Doppler broadening[73].

In plastically deformed metals, positrons are trapped at dislocations. The trapping of positrons in dislocations occurs in two stages[74]. Initially, the positron is weakly localized at the dislocation line, representing a shallow positron trap. The positron then rapidly diffuses along the dislocation line (through pipe diffusion) and is eventually trapped and annihilated in a vacancy bound to the dislocation. Owing to the compressive elastic stress field created by the dislocation, it becomes energetically favourable for the vacancy to bind to it. As a result, the lifetime of positrons annihilated in dislocations is typically slightly shorter compared with that for bare vacancies as the vacancy bound to a dislocation is under compressive stress[75,76]. The positron trapping rate at dislocations is governed by dislocation density, as the positron is first pre-trapped in the dislocation line, which is a line defect with one macroscopic dimension. For these reasons, PAS can be used to determine the dislocation density.

PAS can also be used to study solute clustering, precipitation effects and phase transitions in alloys. Positrons can be trapped in coherent precipitates or solute clusters when the energy of the positrons in these secondary phase particles is lower than in the matrix. This phenomenon is described by positron affinity, which is defined as the sum of the positron and electron chemical potentials[77]. Positrons can only be trapped in coherent precipitates where the positron affinity is more negative than that of the matrix[78]. In the case of semi-coherent and incoherent precipitates, however, positrons are trapped regardless of the affinity at misfit defects created at the interfaces between the precipitates and the matrix, which arise from atomic mismatches[79].

Ceramics

Ceramics are inorganic, non-metallic materials prized for their exceptional thermal, electrical and mechanical properties, and are used in a broad spectrum of applications from biomedical devices and microelectronics to energy storage and production. These polycrystalline materials, characterized by diverse grain sizes, typically consist of oxides, carbides or nitrides synthesized through processes such as pressing, firing and sintering. Owing to their multi-elemental composition, ceramics exhibit a complex defect landscape, ranging from isolated vacancies to mixed-vacancy clusters. Furthermore, their insulating or semiconducting nature implies that these defects can be electrically charged. Positron annihilation studies in this field remain relatively scarce compared to metals or semiconductors.

PAS serves as a powerful tool to characterize porosity, investigate the densification and phase transitions of nanocrystalline phases, and ultimately identify or quantify vacancy-type defects within various ceramic matrices. For example, in yttria-stabilized zirconia compacted nanopowders doped with trivalent chromium oxide, positrons annihilate mainly in vacancy-like defects at grain boundaries or in larger open volume defects most probably located at triple points[80].

Detecting oxygen vacancies (V_O) in oxides using PAS is typically challenging, as these defects are often positively charged, or act as shallow traps that cannot effectively capture positrons. Theoretical calculations show that the positron lifetime in oxygen vacancies is only a few picoseconds longer than in the bulk lattice, with a negligible positron binding energy. However, in $KSr_2Nb_5O_{15}$ photochromic ceramics, oxygen vacancies become detectable through PAS because of the photochromic reaction, which involves neutralization of these vacancies[81]. In the high-temperature superconductor $YBa_2Cu_3O_{7-\delta}$ (YBCO, where $(0 \leq \delta \ll 1)$), ab initio calculations revealed a particularly high positron affinity for the oxygen-deficient plane with the CuO chains that crucially affect the transition temperature, T_c. Using an

energy variable positron microbeam (<50 µm) on epitaxial grown single crystalline YBCO films revealed the spatially resolved variation of the oxygen vacancy concentration in three dimensions, which in turn allowed the determination of the local variation of T_c within the YBCO films[82,83].

Furthermore, by comparing experimental data with ab initio calculations of positron lifetimes and momentum distributions in $SrTiO_3$, V_{Ti} has been identified as the primary intrinsic defect in pure $SrTiO_3$ ceramics[84]. It was also demonstrated that in $Sr_{1-x}La_xTiO_3$, the charge compensation mechanism from lanthanum doping is predominantly governed by the formation of V_{Sr}. From the coincidence Doppler broadening ratio curve measured in Al_2O_3 using pure aluminium as a reference (Fig. 4e), it was shown that annihilation with oxygen 2*p* electrons produces a characteristic signature — a peak at approximately $10 \times 10^{-3} m_0c$ — allowing for the identification of the oxygen chemical environment in oxides.

Understanding irradiation damage in UO_2 is critical, as this ceramic — along with plutonium-doped UO_2 (MOX) — serves as the primary fuel for fission reactors. To directly detect vacancies in UO_2, a slow positron beam coupled with Doppler broadening spectroscopy was used to monitor defect recovery as a function of temperature in Kr-implanted samples[85]. Subsequent experimental studies on alpha-irradiated UO_2 identified a long lifetime component of 307 ± 5 ps (ref. 86), which is higher than the reference bulk lifetime of 169 ± 1 ps measured after annealing at 1,700°C for 24 h in an ArH_2 atmosphere. In helium-implanted UO_2, the Doppler broadening *S* and *W* parameters as a function of helium fluence follow a specific line with a slope — also called the *R* ratio — of around 0.576 ± 0.004 in (*S*, *W*) values measured in 2.5 MeV electron irradiated samples were also aligned on this line[87], suggesting this line could be attributed to the detection of the vacancy defect produced in majority, such as the Schottky vacancy complex V_U2V_O.

These experimental datasets can be interpreted through a comparison with ab initio calculations based on two-component DFT. In UO_2, the strongly correlated U-5f electrons present a major challenge for electronic structure modelling, requiring the inclusion of a Hubbard term (DFT + *U*) in the Hamiltonian to accurately determine positron annihilation characteristics[86,88,89]. In addition, defect relaxation is a critical factor in this material where the ionic nature of the oxide lattice leads to substantial atomic rearrangements upon defect formation or positron trapping. When compared with theoretical annihilation characteristics, PAS remains a vital identification tool. However, its application to this complex material can be challenging because the annihilation signatures — positron lifetimes[86] and the momentum distribution of annihilated pairs[88] — of different vacancy defects can be remarkably similar. For example, the positron lifetimes remain in the 26 ps range for V_U (293 ps), V_UV_O (301 ps) and Schottky defects (304–316 ps), or $2V_U$ (290 ps).

The theoretical momentum distributions are also remarkably similar for V_U and its related complexes such as V_UV_O, V_U2V_O, $2V_U$ and $2V_U2V_O$. This similarity arises because of the strong localization of positron in the V_U (or one of the V_U), making it only slightly sensitive to the surrounding environment or the number of neighbouring oxygen vacancy. By contrast, the $(2V_U2V_O)^{-2}$ complexes exhibit a distinct total momentum distribution and clearly different *S* and *W* values compared with its neutral counterpart. This divergence is driven by a shift in positron localization. In the charged defect, the positron migrates to a position centred between the two uranium vacancies. The similarity in values makes it difficult to differentiate between specific defect types in experimental data, particularly when multiple vacancy species coexist within the material.

Radiation damage

Since the discovery of positron trapping at defects in 1967 (ref. 90), the study of radiation damage has been an important application area of PAS, starting with neutron-induced radiation damage in bulk metals[91,92]. These early measurements revealed the early stages of damage formation, and contributed to the understanding of swelling and deterioration of materials from void formation. The sensitivity of vacancy concentrations down to 10 ppb, combined with positron trapping at single vacancies and small vacancy clusters, make PAS a vital tool to understand the mechanisms that govern radiation damage and evolution of defects induced in collision cascades[20]. Such atomic-scale defects cannot be detected by high-resolution transmission electron microscopy even with recent advancements in electron microscopy techniques[93]. PAS has been extensively used to assess and study radiation damage induced by neutron, electron, light and heavy ion irradiation covering structural nuclear materials and functional materials. The work studying radiation damage in molybdenum[91] and aluminium[92] was followed by several studies on neutron-irradiated iron and copper[94,95], Fe–Cr alloys[96] and steel[97]. Such studies were carried out using positrons from radioactive sources without the need for positron beams, as neutrons produce damage throughout the entire thickness of materials. Studying radiation damage induced by electrons, protons and heavy ion irradiation is possible using slow positrons and variable-energy positron beams[22]. In nuclear material science, ion irradiation is often applied to mimic the impact of neutron irradiation, such as in nuclear reactors, and produce similar damage in a shorter time. PAS was at the forefront to study helium irradiation[98], reveal the formation and characteristics of helium bubbles[99], and study the interactions of helium with irradiation-induced defects using pulsed positron beams[100]. The differences of light-ion and heavy-ion irradiation were also studied[101], and it was determined that heavier ions create larger vacancy clusters.

In semiconductors, ion implantation is the primary tool for doping and tuning electronic transport, which demands detection and characterization of defects induced by implantation and understanding how they affect the electrical properties. PAS is specifically applied to monitor their annealing[102] and identify the optimal temperature and procedure to eliminate compensating defects and unwanted donors or acceptors[103].

Depth-resolved PAS measurements are widely used to investigate ion-induced defects by monitoring changes in defect concentration and vacancy cluster size as a function of irradiation dose and depth. Figure 5a shows the average positron lifetime as a function of implantation depth, illustrating its evolution with increasing displacement per atom from 10^{-4} to 1 displacement per atom revealing the accumulation and growth of vacancy-type clusters within a heterogeneous multiphase metal/oxide structure[93]. PAS can have an important role in revealing mechanisms of defect formation and interactions with the microstructure and chemical surroundings. Recent work has shown how positron methods can be used to reveal the short-range order induced by irradiation in high entropy alloys[104] and the mechanisms of interactions of collision cascades with voids in materials[105]. Segregation of atomic-scale solutes into defect complexes cannot be detected by high-resolution imaging techniques[106], or even atom probe tomography, but can be easily revealed using coincidence Doppler broadening spectroscopy[107], with the additional ability of detecting radiation-induced ultrafine precipitates[108]. With ongoing efforts to develop in situ PAS during irradiation[109], positrons are expected to have a greater role in understanding radiation damage in the emerging

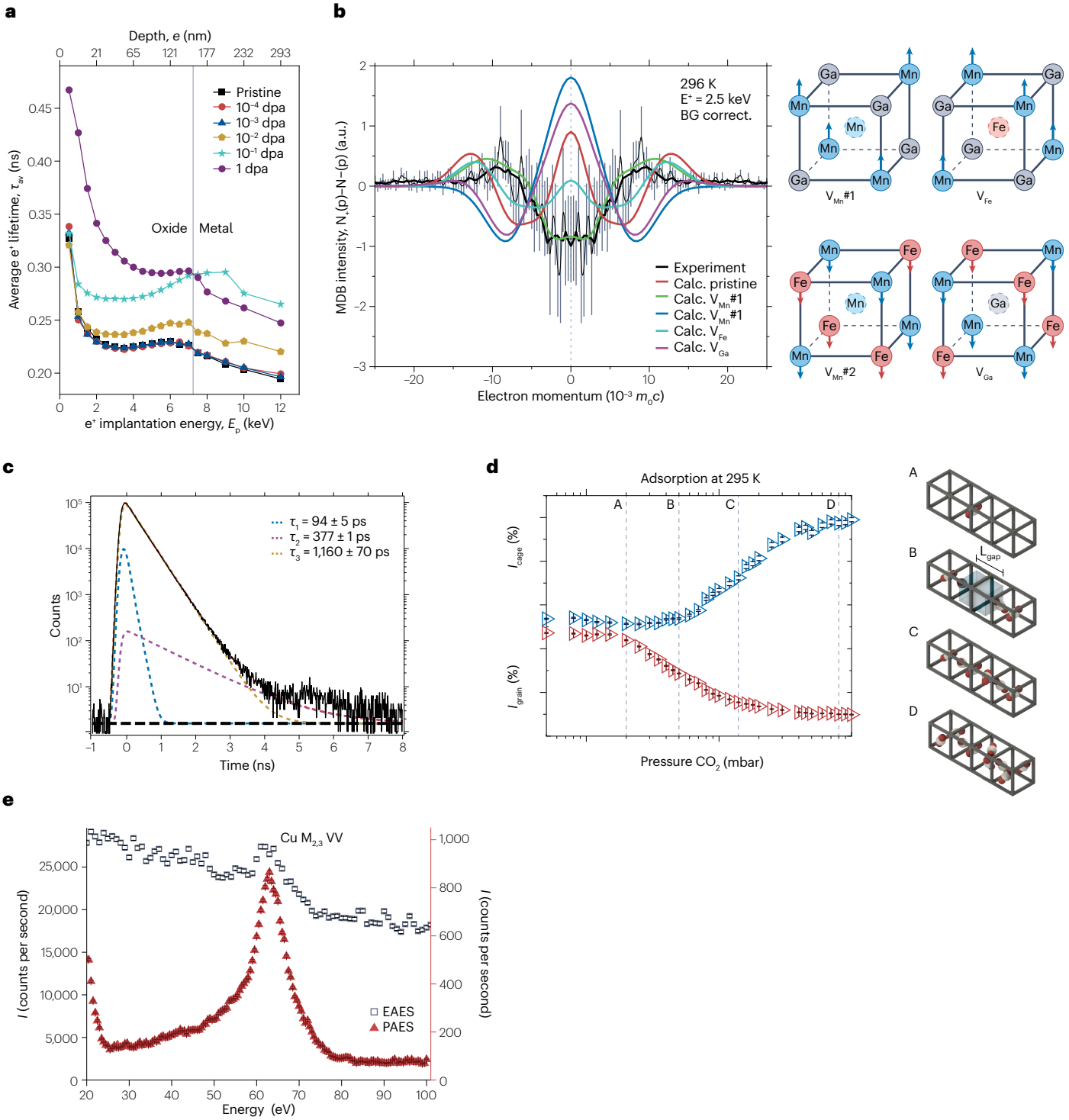

Fig. 5 | Examples of positron lifetime and Doppler broadening data in metal oxides, ordered metal alloys, perovskite thin films and metal–organic frameworks. a, Evolution of the average positron lifetime, τ_{avg}, and implantation depth, z, as a function of positron implantation energy, E_p, for multiphase metal/oxide samples with various displacement per atom (dpa). **b**, Magnetic Doppler broadening (MDB) spectra in Mn_2FeGa with vacancies (V). **c**, An example positron lifetime spectrum, where I is intensity, measured from a $(Cs_{0.15}FA_{0.85})Pb(I_{0.92}Br_{0.08})_3$ thin film, where FA is formamidinium. The decomposition is separated into three lifetime components (94 ± 5 ps, blue; 377 ± 1 ps, purple; and 1,160 ± 70 ps, yellow). **d**, Intensity (I) of positronium trapped inside metal–organic framework cages and on grains, as a function of CO_2 pressure. L_{gap} is the average gap length. **e**, A comparison of positron annihilation-induced Auger electron spectra (PAES) and electron annihilation-induced Auger electron spectra (EAES). a.u., arbitrary units. Part **a** adapted with permission from ref. 93, Elsevier. Part **b** adapted from ref. 121, CC BY 4.0. Part **d** adapted from ref. 146, CC BY 4.0. Part **e** adapted with permission from ref. 170, Elsevier.

materials for extreme environments and guiding the design of novel material systems.

Magnetism and spin-polarized phenomena

Positrons emitted through β-decay are naturally spin-polarized longitudinally due to parity violation in the weak interaction regime[110]. This intrinsic property offers a unique opportunity for positron-based investigations of magnetism, including various spin-related phenomena. From the dawn of PAS in the 1960s, ferromagnetic band structures have been studied using the ACAR method with polarized positrons[111,112]. Whereas research on bulk ferromagnets was progressing along this line, a spin-polarized positron beam for investigating top-surface magnetism was demonstrated in the late 1970s[113]. By using energy-tunable positron beams and conventional sources in combination with established PAS techniques, electron spins can be selectively probed at various depths, including the topmost surface layer, buried interfaces in thin films and deep bulk regions. Regarding spin detection at atomic vacancies, no alternative methods currently offer comparable sensitivity or feasibility.

The basic concept of spin-polarized PAS (SP-PAS) relies on spin-dependent annihilation, either between a free positron and an electron, or from a positronium state[114]. By observing changes in the number of two-γ and three-γ annihilation events (singlet versus triplet), as well as variations in the electron–positron momentum distribution and annihilation lifetime depending on the spin orientation, the spin states of electrons can be detected.

A ferromagnet exhibits two distinct positron annihilation rates depending on whether its magnetization is parallel (+) or antiparallel (−) to the positron spin polarization

$$\lambda_{\pm} = \frac{1 \pm P_{+}}{2}\lambda^{\uparrow} + \frac{1 \mp P_{+}}{2}\lambda^{\downarrow} \tag{5}$$

where $\lambda^{\uparrow}$ and $\lambda^{\downarrow}$ are the annihilation rates for spin-up and spin-down positrons, respectively, and P_{+} is the positron spin polarization. With $\lambda_{\pm}$, the combined annihilation rate, measured by lifetime spectroscopy and known P_{+}, one can determine $\lambda^{\uparrow(\downarrow)}$, which is directly comparable to the DFT calculation. Similarly, the electron–positron momentum densities are given by

$$\rho_{\pm}(\mathbf{p}) = \frac{\lambda_S(1 \pm P_{+})}{4\lambda^{\uparrow}} \sum_{i=1}^{\text{occ.}} \rho_i^{\downarrow}(\mathbf{p}) + \frac{\lambda_S(1 \mp P_{+})}{4\lambda^{\downarrow}} \sum_{i=1}^{\text{occ.}} \rho_i^{\uparrow}(\mathbf{p}), \tag{6}$$

where $\rho_i^{\uparrow(\downarrow)}(\mathbf{p})$ is the momentum densities of majority/minority spin electrons of ith band, $\lambda_S = 4\pi r_e^2 c$ and the summation is applied to all the occupied states. The spin-dependent momentum distributions of both perfect crystals and vacancies can be studied by Doppler broadening and ACAR spectroscopies.

The difference of Doppler broadening spectra between positive and negative magnetization is referred to as the magnetic Doppler broadening (MDB) spectrum[115,116]. The amplitude of an MDB spectrum increases in the order of magnetization. For example, 2D-ACAR spectroscopy revealed the Fermi surfaces of the majority and minority spin bands of the Cu_2MnAl Heusler alloy[117]. Similar work was also carried out for NiMnSb, which is a half-Heusler alloy with structural vacancies[118]. These results provide insights into half-metallicity, which is crucial in the fabrication of spin devices.

SP-PAS has also been applied to oxide and nitride materials for semiconductor spintronics[119,120]. In gadolinium-implanted or doped GaN, defect complexes involving gallium vacancies and gadolinium atoms are considered the primary source of ferromagnetism. However, against this expectation, vacancy clusters are implied to have an important role in the emergence of ferromagnetism than the defect complexes. SP-PAS was also used to identify the species of vacancies in ferrimagnetic Mn_2FeGa. The comparison of experimental and computational MDB spectra show a near-perfect match for a manganese vacancy surrounded by manganese and iron atoms[121] (labelled V_{Mn}#2 in Fig. 5b). The detection of interface spin polarization has also been attempted using variable-energy spin-polarized positron beams. At the MgO–FeSi interface, excess spins are confined at the interface[121]. Given the importance of interface spin in various device applications, further utilization of the SP-PAS method is anticipated.

Surface spin polarization may be evaluated through the annihilation of positronium emitted into vacuum. A remarkable feature of this method is its extremely high sensitivity to the topmost surface, because positronium is formed exclusively on the vacuum side of the surface. Three-γ annihilation of spin-triplet (*ortho*) positronium gives rise to characteristic long lifetime (142 ns) and the continuous energy spectrum below 511 keV. The change in the three-γ intensity upon spin reversal is proportional to the spin polarization of electrons (P_{-}) as

$$\frac{I_{Ps}^{3\gamma}(+) - I_{Ps}^{3\gamma}(-)}{I_{Ps}^{3\gamma}(+) + I_{Ps}^{3\gamma}(-)} = \frac{2\varepsilon(1) - \varepsilon(0)}{2\varepsilon(1) + \varepsilon(0)} P_{+} P_{-} \cos\phi, \tag{7}$$

where $I_{Ps}^{3\gamma}$ is the three-γ intensity, the sign ± means that the polarization vectors of positrons and electrons are parallel or antiparallel, ε(1,0) is the detection efficiency depending on the magnetic quantum number ($m_s = 1$ or 0) of spin triplet positronium and φ is the angle between the polarization vectors of positrons and electrons[122].

Spin polarization effects induced at heavy metal surfaces — due to the giant spin Hall and Rashba effects[123–125] — as well as those arising from the magnetic proximity effect in graphene or ferromagnet systems[126,127], have been investigated. For example, as the spin polarization of graphene placed atop a ferromagnet is not accessible via angle-resolved photoemission spectroscopy, a widely used technique for probing surface electronic states, the role of SP-PAS becomes particularly notable[128]. Measurement of spin-dependent positronium annihilation provides only an average spin polarization of all electrons participating in positronium formation, due to its lack of energy selectivity. This limitation was addressed by developing spin-polarized positronium time-of-flight spectroscopy[129]. In fact, with this method, negative spin polarization near the Fermi level was confirmed for the Ni surface[130].

Organic–inorganic lead halide perovskites

Organic–inorganic lead halide perovskite thin films are promising as functional light-conversion layers in solar cells, owing to the rapid increase in record solar cell efficiencies in the past 15 years. The ABX_3 perovskites contain two types of cations, A and B, and one type of anion X. The A-site cations are 12-fold coordinated with anion neighbours in a large cuboctahedron, whereas the B-site cations are 6-fold coordinated with anion neighbours at the edges of a octahedron with a smaller volume. As the positron lifetime is sensitive to the size of the open volume of defect, it has been used for analysing cation vacancy defects on the A and B sites both in traditional perovskites such as $SrTiO_3$ (refs. 84,131,132) and in organic–inorganic perovskites such as $MAPbI_3$[133], with the organic molecule methylammonium (MA). Comparison with DFT calculations shows that the A-site vacancy (V_{Sr} or V_{MA})

exhibits a longer positron lifetime than that of the B-site vacancy (V_{Ti} or V_{Pb})[131,133], enabling discrimination between these two types of monovacancies. Lead vacancies that act as deep level acceptor defects were found in $MAPbI_3$ thin films[133]. The individual concentrations of the two cation vacancies can be extracted in the range starting from ~0.1 ppm and up to ~50 ppm corresponding to the case of saturation trapping of positrons in these vacancies, well below the ~1% detection limit of transmission electron microscopy.

The combination of positron lifetime with coincidence Doppler broadening spectroscopy can be used to gain deeper understanding of the local chemical environment, as shown for $MAPbBr_3$ and $CsPbBr_3$ single crystals[134]. Comparison with DFT calculations of the positron lifetimes and of ratio curves (relative to aluminium) of the CDB electron–positron momentum distributions indicated annihilation in defect-free bulk perovskite lattice. Other PAS studies did find the presence of cation vacancies in $MAPbBr_3$ single crystals[135], in which the concentration of methylammonium vacancies is suppressed in MABr-rich single crystals compared with stoichiometric $MAPbBr_3$, leading to the detection of lead vacancies only.

Doppler broadening *S*-parameter depth profiling can be used to examine the stability of the perovskite crystal phase in thin films. Thin films of $FAPb(I_{1-x}Br_x)_3$ (where $0 \leq x < 1$ and FA is formamidinium), exhibit enhanced stability compared with $FAPbI_3$ upon substitution of iodine by bromine at $x \sim 0.05$, and a higher solar cell efficiency of 17.1% for $FAPb(I_{0.95}Br_{0.05})_3$ was achieved compared with 13.6% for $FAPbBr_3$ (ref. 136). The corresponding Doppler depth profiles revealed a decrease in the *S* parameter, caused by a reduction in the concentration of vacancies[136]. *S*-parameter depth profiling is also capable of monitoring the time-dependent degradation of organic–inorganic lead halide perovskite films due to long-term exposure to ambient air and subsequent infiltration of moisture, for example[137]. A large reduction in layer thickness of $MAPb(I_{1-x}Br_x)_3$ thin films is seen during air exposure for up to 22 days, caused by the formation of dense PbI_2 and the release of volatile reaction products such as HI and I_2 from the film. Ultrathin (less than 1-nm thick) Al_2O_3 cap layers slow down and reduce the degradation[137]. Figure 5c shows a representative positron lifetime spectrum measured for $(Cs_{0.15}FA_{0.85})Pb(I_{0.92}Br_{0.08})_3$ with decomposition into three lifetime components (94 ± 5 ps, 377 ± 1 ps and 1,160 ± 70 ps) that highlight the high vacancy content.

From the theoretical perspective, DFT calculations of positron lifetimes consistently report the trend of $\tau_{V_A} > \tau_{V_B} > \tau_{bulk}$ for various organic–inorganic lead halide perovskites[131,133–135,138,139]. Recent advances in ab initio calculations consider the choice of the appropriate electron–positron correlation functional and the impact of polymorphism[139]. For example, the use of more advanced approximations leads to the prediction of a stronger positron binding in lead vacancies compared to methylammonium vacancies[139].

Metal–organic frameworks

Metal–organic frameworks (MOFs) are porous crystalline coordination networks composed of metal nodes and organic linkers[140]. MOFs display complex hierarchies of microporosity and mesoporosity. Their functionality, such as for gas storage, separations or catalysis, for example, is dependent on the pore sizes and architecture, including their interconnections and host–guest interactions. Characteristics of materials in this area can be achieved using PAS-based positron porosimetry[141], which complements conventional porosimetry (such as N_2 adsorption). Several advantages in using PAS include negligible influence of the probe (typically o-Ps) on the material[142], particularly important for flexible MOFs, sensitivity to subnanometre free volumes and closed pores[142–144], the ability to conduct tests under almost any external conditions (such as temperature, pressure, presence of various gases or vapours)[145,146], and the ability to detect subtle changes due to phenomena affecting o-Ps (such as migration or quenching), although this requires careful interpretation[146,147].

As in most complex porous systems, several o-Ps components are observed in MOFs – typically two[142,144–149] or three[150–153]. Underestimating their number often leads to averaging and obtaining incorrect pore sizes. This may be caused by setting the spectrometer time base too short (≪1 μs), which truncates components with lifetimes of several tens of nanoseconds. However, sometimes this can also be caused by too few counts (≪10 million), when components are masked by statistical noise. Even when both conditions are met, it is worth initially estimating the number of components using an algorithm such as maximum entropy for lifetime (MELT) analysis that does not require a priori assumptions[154]. However, owing to the limitations of MELT[155], it is best to adjust the number of components, which can vary with temperature or pressure, to obtain continuous trends in lifetimes and intensities.

The longest lifetime in MOFs almost always exceeds 20 ns, and the conventional Tao–Eldrup model[156,157] is insufficient to determine pore size. Furthermore, the shape of the free volume differs greatly from the sphere assumed in the Tao–Eldrup model. The extended model[158,159] analyses the lifetime in the infinitely long cylindrical free volume as an average weighted by Boltzmann distribution over Ps energy levels, labelled by *n* and *m*, in a potential well of radius, *R*, approximated by the infinite potential well with an extended radius $R + \Delta$

$$\tau = \frac{\sum_n \sum_m g_m e^{\frac{-h^2 Z_{nm}^2}{16\pi^2 m_e (R+\Delta)^2 kT}}}{\sum_n \sum_m g_m \lambda_{nm} e^{\frac{-h^2 Z_{nm}^2}{16\pi^2 m_e (R+\Delta)^2 kT}}}, \tag{8}$$

where Δ depends on the material, g_m is the statistical weight of the *m*th state ($g_0 = 1, g_{m>0} = 2$), *h* is Planck's constant, m_e is the electron mass, *k* is the Boltzmann constant, *T* is the temperature and Z_{nm} is the *n*th node of the Bessel function of first kind $J_m(r)$. The annihilation rate at level *nm* is

$$\lambda_{nm} = \lambda_p P_{nm} + \lambda_i (1 - P_{nm}) \tag{9}$$

where λ_p is pick-off annihilation rate approximated in the model by 2 ns^{-1} and $\lambda_i = 7\ \mu s^{-1}$ is the intrinsic o-Ps annihilation rate. The probability, P_{nm}, of finding Ps outside the zero-electron density region ($r < R$) is

$$P_{nm} = \frac{\int_{\frac{R}{R+\Delta}}^{Z_{nm}} J_m(r)^2 r dr}{\int_0^{Z_{nm}} J_m(r)^2 r dr}. \tag{10}$$

The extended Tao–Eldrup model is facilitated by calculation programs[160]. It is also recommended to choose the geometry that best suits the MOF under study (which will still be a considerable approximation given the open structure of these materials). Careful selection of the Δ parameter is also important; it should be lower than 0.18 nm in silicas, and perhaps even lower than the typical 0.166 nm determined for molecular crystals[161]. A shape-free model has also been

recently presented, and shows good agreement with a wide range of measurements[162].

The final challenge is to correctly interpret the origin of the components and their changes. It is crucial to recognize that, in addition to pick-off annihilation, Ps may be influenced by additional processes. A particularly important contribution comes from o-Ps migration from smaller to interconnected larger pores[163]. The migration in MOFs depends strongly on the crystallite size[152] in powder samples or positron implantation energy in thin films[149]. Owing to the regular structure of MOFs, instead of being trapped in a specific pore, o-Ps can remain in delocalized Bloch states extended over large volumes of the crystal[146,148], as postulated for zeolites[164]. Some Ps in Bloch states can localize beyond grain boundaries[146]. Migration from both localized and delocalized states results in distortion of pore-size estimated obtained using extended Tao–Eldrup models, but also provides a unique insight into the processes occurring in MOFs, such as during gas adsorption. In turn, the presence of metal nodes may result in Ps quenching or inhibition, which should be considered, but this process applies only to some MOFs[147].

Taking the above issues into account enables the effective use of positron porosimetry to study the properties of MOFs in various applications including network closing effects[142], dye adsorption[151], water adsorption[153] with the prospect of desalination[150], and especially promising CO_2 capture — from the first application of PAS for studying MOFs[145] to in situ studies of almost ready-to-use materials[146]. Figure 5d shows the results from this latter work where the intensity of positronium trapped inside the cages of the MOF and outside its grains varies as a function of CO_2 pressure. Interpreting PALS measurements, in particular the intensities of o-Ps trapped in the MOF cages and outside its grains, allowed reconstruction of the localization of CO_2 particles in the CALF-20(Zn) network at different pressures.

Surfaces and interfaces

The defining characteristic of PAES is that its signal originates almost exclusively from the top-most atomic layer, established through studies of palladium overlayers on Cu(100). At 173 K, deposition of approximately one monolayer of palladium caused the palladium PAES signal to saturate, whereas the copper signal attenuated to near zero, demonstrating that subsurface atoms do not contribute detectably to the PAES spectrum[165]. Upon warming to 303 K, changes in the PAES intensities provided direct evidence for thermally activated intermixing between copper and palladium in the topmost layer. At 423 K, the formation of a copper overlayer was observed, driven by segregation. These experiments established PAES as a direct probe of temperature-driven surface diffusion and alloying dynamics. The top-layer surface selectivity of PAES has made it useful in multiple studies of surface diffusion[166], identification of adsorption sites on composite surfaces[167] and annealing-induced changes in morphology[168]. Time-resolved PAES enables the investigation of the dynamics of surface atoms and the in situ observation of segregation processes. The Cu/Pd system was studied using PAES on palladium substrates coated with 2.88 and 5.77 monolayers of copper. The time constant for segregation was experimentally determined as 1:38 (± 0:21) h and the final segregated configuration was found to be consistent with theoretical calculations[169,170].

The elimination of background in PAES (Fig. 5e) enables several important applications, including the first direct measurements of extremely low-energy Auger processes. This approach was used to observe the carbon–VVV transition in graphene, where V indicates a valence band electron[171]. The resulting low-energy peak near 4 eV matched theoretical expectations and showed that most deep valence holes (approximately 80–100%) decay via a VVV Auger process that only involves valence electrons. This same method was applied to identify the oxygen 2*s*–VV transition (an LVV transition where the hole is created on the L-electron level in oxygen, and the rest of the process involves electrons in the valence band, denoted as VV) on oxygen-covered metals and oxides, a feature never cleanly observed by traditional Auger techniques because its low energy, below ~10 eV (ref. 172). With the background removed, a distinct low-energy peak associated with oxygen 2*s* hole decay was revealed, and comparison with theory showed that the oxygen LVV transition occurs with high efficiency, nearly matching that of the oxygen KVV process (a transition similar as LVV, but the hole is created on a K-electron level in oxygen). Together, these studies illustrate how background-free PAES provides a uniquely sensitive window into very low-energy Auger channels that are otherwise inaccessible.

Gamma–Auger coincidence spectroscopy is a distinctive application of PAES enabled by the fact that each PAES Auger peak arises from a single, well-defined core level. As core-hole creation is tied directly to the annihilation event, selecting a given PAES peak isolates annihilations involving a specific orbital. Measuring the Doppler-broadened annihilation γ spectrum in coincidence with electrons from that peak yields the momentum distribution of the electron–positron pair associated with that orbital. As Doppler broadening reflects the electron momentum, the resulting γ-line shape becomes an orbital-resolved momentum signature. Early studies showed that gating on transitions such as $CuM_{2,3}VV$, $AgN_{2,3}VV$ and $AuO_{2,3}VV$ produces Doppler spectra in excellent agreement with relativistic calculations, establishing the approach as a sensitive probe of many-body and electron–positron correlation effects[173,174]. Recently, a 2D time-of-flight (ToF) PAES–Doppler coincidence spectrometer was used to record a full correlation map between electron flight time (and thus energy) and γ-ray Doppler shift[175]. This enabled extraction of annihilation line shapes for both outer-core orbitals (such as copper 3*p*) and deep core states including carbon 1*s* and oxygen 1*s*, even in heterogeneous systems such as graphene/copper. By selecting electrons in ToF ranges corresponding to carbon KVV, oxygen KVV or the 7–25 eV low-energy region, it was demonstrated that low-energy Auger electrons originate largely from deep-valence or shallow-core holes and are coincident with γ rays exhibiting small Doppler shifts, consistent with annihilation with low-momentum electrons. Higher-energy Auger peaks (such as $M_{2,3}VV$ and KVV transitions) correlate with broader γ-ray line shapes characteristic of high-momentum core electrons. Fitting these line shapes to ab initio orbital momentum densities allowed identification of the orbital composition of the annihilation signal and clarified which initial holes produce specific features of the PAES spectrum. Together, these results establish γ–Auger coincidence spectroscopy as a powerful orbital-selective probe that enables quantitative tests of many-body theory and clear identification of the mechanisms underlying both high- and low-energy Auger emission.

The surface selectivity of PAES — arising from the trapping of positrons at the surface prior to annihilation — suggests that Doppler-broadening spectroscopy may likewise yield element-specific surface information. Coincidence Doppler-broadening spectroscopy can provide chemically specific signatures from the topmost atomic layer, even when positronium formation and reduced core-electron overlap diminish the core-annihilation signal[176]. By simultaneously acquiring PAES data from clean, adsorbate-covered

and thin-film-coated copper, silver and gold surfaces, it was shown that the high-momentum region of the annihilation line shape remains highly sensitive to elemental identity. Ratio-curve analysis — in which experimental Doppler spectra are normalized to clean copper and fitted with linear combinations of ab initio momentum distributions — yields quantitative surface compositions that agree well with PAES for simple systems and reliably detect submonolayer adsorbates and single-layer overlayers. As 511 keV γ-rays escape readily from buried or enclosed regions, the work establishes coincidence Doppler broadening as a promising complement to PAES for in operando studies of otherwise inaccessible internal or porous surfaces.

Reproducibility and data deposition

A properly tuned positron lifetime spectrometer produces lifetime spectra where the average positron lifetime can be determined with 0.2 ps accuracy (as determined by the standard deviation over tens of successive experiments)[103]. Variations between spectrometers and source corrections (for different sources) may result in an offset of up to 5 ps, making direct comparisons of lifetime values between laboratories challenging. This baseline offset is mitigated by utilizing reference samples where positrons are not trapped at vacancy defects for each studied material and therefore annihilate in the free state of the lattice (also called the bulk). This is also the basis of comparison with theoretical calculations where the variation baseline offset originates from the necessary approximations in calculating the electron and positron states. The ISO technical specification for evaluation of pore size in materials by free volume sizes was recently determined through the quenching of the o-Ps pick-off annihilation process[177].

In addition, for Dopper broadening and ACAR experiments, the momentum parameters depend strongly on the detector geometry, resolution, calibration and amplifier properties, therefore necessitating comparative measurements. It is typical to express the S and W parameters as normalized to the S_B and W_B obtained in a reference sample. This reduces the dependence of the data on the various aspects listed above to some extent, but not completely[178]. Full analysis and interpretation of the results are necessary before comparing results from different laboratories. The analysis of ratio curves obtained from either CDB or ACAR experiments is most often performed by comparison with theoretical calculations, giving the possibility of more detailed interpretations of the physical processes.

Limitations and optimizations

Positron annihilation methods are powerful for identifying, quantifying and determining the physical characteristics of point-like vacancy defects in elemental metals and semiconductors, as well as in simple binary compounds and dilute alloys. Most detailed information can be obtained for mono-vacancy and di-vacancy defects, with the sensitivity to the exact size and detailed atomic surroundings gradually decreasing with the increase of the size of the open volume. o-Ps annihilation-based methods have the highest sensitivity for free volume structures of about 2 nm in diameter. However, detailed defect identification with positron annihilation methods becomes particularly challenging when the complexity of the studied material increases. In two-component compounds, where the crystal structure contains non-identical lattices sites for one type of atom, such as β-Ga_2O_3 that has two non-equivalent Ga sites and three non-equivalent O sites, the identification becomes difficult owing to the multitude of similar, but not identical, possible defects. When the number of elements in the compound or alloy is increased, the number of different point defects and their combinations increase rapidly. In elemental materials and simple (nearly) covalently bonded binary compounds, typically one type of defect is clearly dominant, whereas in complex materials there is a tendency for coexistence of many types of point defects with concentrations high enough to be detected in experiments. Finally, the more complex the materials, the more difficult it seems to make a suitable reference sample in which the overall defect concentrations would be low enough for the material to considered defect-free from the perspective of the positron experiment.

Outlook

PAS is a comparative technique where the detailed identification of defects relies on comparison with a well-defined reference sample of the same material that does not exhibit positron trapping at vacancies. For many novel and complex materials, such samples do not exist, making the defect identification challenging[179,180]. Synthesis conditions of the material in question, such as stoichiometry, temperature or doping level, affect the final defect distribution in the samples via thermodynamic and kinetic processes. Using different temperature, illumination, electric and magnetic fields for selective defect excitation is important. Transient experiments where sub-bandgap illumination and biasing have been used in pump–probe mode[40,181] can be used to elucidate the dynamics of charge trapping and emission processes in semiconductors, but these types of experiments have not become more common[182]. Reducing the need of having two thick enough samples for the sample–source–sample sandwich type experiments by using anti-coincidence techniques may allow easier experiments in thin films[183,184]. For identifying defects in materials with ever more complex lattice structures, the experimental sophistication needs to be maximized. Improving the selectivity of the positron annihilation signals would strongly benefit studies of alloyed systems as well as complex lattice structures with several inequivalent lattice sites. One possibility could be using characteristic X-rays emitted after positron annihilation with core electrons for direct specification of the origin of the annihilation signal in near-surface experiments. Measurements of γ-rays and X-rays in coincidence should not be an obstacle.

Using spin-polarized positron beams merits further development. Spin-polarized positrons are a unique tool for investigating spin-related phenomena in spintronic and quantum materials and may have an important role in exploring homochirality in biological systems[121,185]. However, several technological challenges must be acknowledged. Differences in the annihilation lifetimes and ACAR or Doppler broadening spectra upon magnetic field reversal are generally subtle, requiring highly precise and stable measurements[129]. Further improvements in both time and energy resolution are essential, particularly for positron spin-relaxation spectroscopy[186], which currently remains impractical for directly observing time-dependent spin precession due to its stringent requirement of sub-10-ps time resolution. For surface spin polarization, positronium spectroscopy[187] is especially valuable owing to its exceptional sensitivity to the outermost atomic layer, potentially compensating for limitations inherent in photoemission spectroscopy. Although energy-resolved surface positronium spectroscopy[130] has demonstrated the ability to probe spin-polarized surface density of states, further development towards an angle-resolved variant is awaited to enable direct observation of spin-polarized band dispersions. The development of efficient positron spin filters remains a compelling research direction, and the establishment of facility-based, highly spin-polarized and intense positron sources/beams is strongly desired to support future advanced investigations[188]. Integration with positron-induced Auger electron spectroscopy could allow correlated photon–electron

measurements, and quantum materials research promises to further expand the impact of positron annihilation methods.

Although (two-component) DFT has been the workhorse for calculations of positron interactions in condensed matter, it relies on input in the form of the correlation energy and enhancement factors to attempt to account for short-range correlations for the positron in electron gas (rather than the real material environment), which can lead to spurious effects in the spectra and show deficiencies. An important recent advance was the development and application of quantum Monte Carlo to positrons annihilation in bulk[189,190], demonstrating that parameter-free many-body theory descriptions are feasible. These calculations, based on variational and diffusion quantum Monte Carlo, are computationally very expensive and have been applied so far for positrons in solids within the pseudopotential approximation, in which only valence electrons are treated explicitly. A clear benefit of this approach is the inherent linear scaling of the Monte Carlo method in which the positron lifetime[189] (for silicon, diamond carbon, AlN and lithium) and Doppler broadening of annihilation radiation for semiconductors and insulators (such as silicon and AlN) are both considered[190]. Apart from the overestimated positron lifetime in the silicon lattice, the results are in very good agreement with experiments, and free of parametrized input, unlike DFT results that are essentially determined by the choice of the enhancement factor.

Another powerful framework for describing positron interactions with many-electron atoms or molecules — and allows for the inclusion and study of correlations in a natural, transparent and systematic way — is diagrammatic many-body theory[191]. In this Green's function-based approach, rather than solving the full wavefunction of the N-electron and positron wavefunction, amplitudes for processes of interest, such as positron annihilation with a bound electron, are described via diagrammatic series. The dominant diagrams that describe polarization, screening and virtual-Ps formation can be calculated non-perturbatively via resummation[191]. The annihilation amplitude and momentum density also admits a diagrammatic expansion that includes corrections to the annihilation vertex that describe the short-range electron–positron interactions. The many-body theory thus allows for ab initio account of these interactions and exact calculation of enhancement factors[192]. The approach has provided a complete understanding of positron scattering, annihilation and cooling in noble gas atoms[34,192–194], accurate ab initio description of positron binding and direct annihilation in molecules[191,195], and also been extended to Ps annihilation in atoms[196,197]. The method and its computational implementation in the EXCITON+ code[191] is, in principle, applicable to positron interactions in clusters and condensed matter. In particular, so-called GW calculations, which describe the positron propagating in the screened interaction with the crystal, should be feasible, allowing ab initio calculation of band structure, positron localization, annihilation rates and γ-spectra. The methodology can also be extended to enable theoretical description of Ps scattering and annihilation, and with molecules, relevant to Ps imaging.

Embedding strategies are also emerging as a promising route to balance accuracy and computational feasibility[198]. By treating the positron and its local electronic environment with high-level many-body methods while embedding this region within a lower-cost electronic structure description, embedding approaches could enable accurate modelling of positron trapping and annihilation without sacrificing scalability.

The calculation of material and defect-specific positron trapping rates in insulators and semiconductors as a function of the defects' charge states and temperature should be further developed to a predictive ab initio level. This would allow an improved understanding of how different defects and charge states compete in positron trapping in realistic experimental conditions. The existing models[199] are limited to model potentials and a simplified band model of silicon. The positron trapping channels are similar to charge carrier trapping and recombination processes occurring in semiconductors. For example, trap-assisted Auger–Meitner recombination (an electronic process) and non-radiative carrier capture via multiphonon emission can both be described using DFT-based methods[200,201]. Similar models should be developed for corresponding electronic/positronic and phonon-mediated positron trapping channels. Recent developments in the ab initio description of the coupling of electronic and phononic degrees of freedom[202,203] give promise that the many-body approach can be extended to include the coupling between positron and phonons and reveal any effects of this on positron localization in defects.

Advancements to atomic and molecular physics

Traditionally, PAS is used to study condensed-phase systems. However, over the past 25 years, a new approach has emerged, in which positron annihilation is used to probe the structure and vibrations of polyatomic molecules. This adaptation makes use of high-resolution (40 meV and better) trap-based positron beams whose energy can be tuned in the range from a few tens of meV to eV energies[204,205]. This enables energy-resolved measurements of positron annihilation rates in gas-phase molecules[206]. Experiments revealed a complex structure of vibrational Feshbach resonances, which are characteristic of the process of positron attachment accompanied by vibrational excitations[207]. These resonances are responsible for orders-of-magnitude enhancements of positron annihilation rates in polyatomic molecules, a phenomenon that was known from pioneering experiments on Ps[208], but took nearly half a century to understand properly[209–211].

The energy-resolved annihilation rate with resonant peaks and other features covering the range of molecular vibrational modes represents a molecule-specific annihilation spectrum[212]. Energy shifts of the resonances provide information on positron-binding energies, which have now been measured for over 100 molecules[213]. These data reveal a strong dependence of the binding energy on global molecular properties, such as the dipole polarisability and dipole moment (for polar species), but also on the number of π bonds. Experimental data stimulates developments of new theoretical approaches for describing strongly correlated positron interaction with molecular electrons. In particular, the new many-body theory method[191] holds promise for being the most accurate approach in this problem, while also providing quantitative understanding on the role of correlations, molecular properties and symmetry, and predictive capability[195].

The strongest vibrational Feshbach resonances in the annihilation spectra are often linked with infrared-active vibrational modes for which there is a clear coupling mechanism[214]. However, positrons can also attach by exciting non-dipole vibrational modes[215]. In addition, there is clear evidence of positrons being capable of exciting a very dense quasicontinuous spectrum of multimode vibrational resonances[216] and other effects of mode coupling[217] due to anharmonic vibrational interactions. Enhanced positron annihilation is strongly linked with the ubiquitous phenomenon of intramolecular vibrational energy redistribution. Intramolecular vibrational energy redistribution is at the heart of all fundamental chemical transformations including the making and breaking of bonds, and positron annihilation provides a unique probe of this complex phenomenon. Combined efforts of theory and experiment also reveal that positron binding is

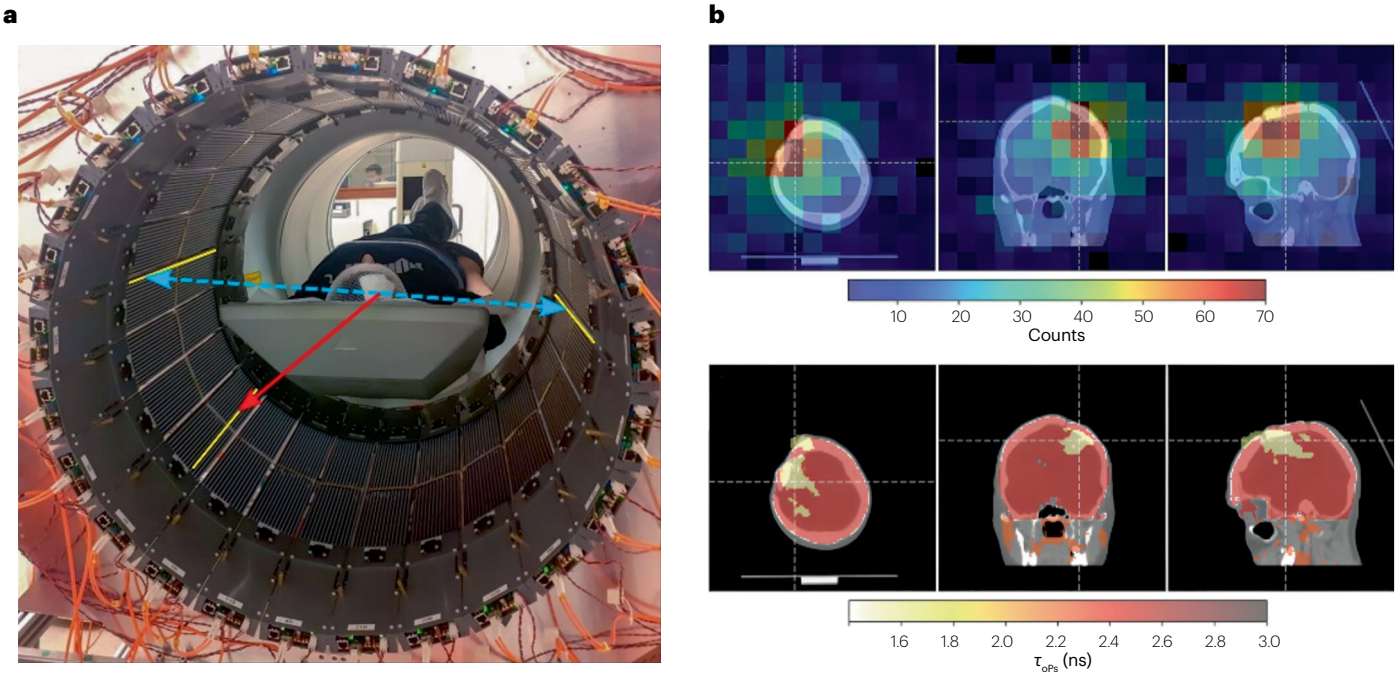

Fig. 6 | Positronium imaging with positron emission tomography. A photograph of the patient in the first multiphoton tomograph (J-PET, panel **a**) used to generate positronium images (panel **b**). The patient diagnosed with brain glioma was administered with pharmaceuticals labelled with the ^{68}Ga radionuclide, which emits positrons and prompt γ-rays ($^{68}Ga \rightarrow {}^{68}Zn^* + e^+ + \nu \rightarrow {}^{68}Zn + \gamma + e^+ + \nu$, where e^+ is a positron and ν is neutrino). The dashed blue arrows on the J-PET represent photons from electron–positron annihilation and the solid red arrow the prompt γ-ray from the de-excitation of the ^{68}Zn* radionuclide. Their detection locations are highlighted in yellow[242]. The first clinical positronium images of the head of a patient with recurrent secondary glioblastoma (panel **b**) were obtained in the year 2024. The top images show the standard PET image and the bottom images show τ_{oPs}, the mean *ortho*-positronium lifetime. Adapted from ref. 242, CC BY 4.0.

sensitive to molecular geometry, used, for example, to distinguishing isomers in halogenated species[218] or to probe molecular conformation of long-chain alkanes[219]. The latter system demonstrates that positron binding and annihilation resonances can serve as a probe of the internal molecular vibrational temperature.

Positronium imaging in PET

The first clinical application of positrons in medical diagnostics was demonstrated in 1953 (ref. 220), only 21 years after the discovery of positron. In that study, the patient with an intracranial recurrence of the meningiomatous tumour was injected with the ^{74}As radionuclide that emits positrons. The 511-keV photons from positron–electron annihilation in the patient's brain were registered in coincidence by two sodium iodide crystal scintillators positioned collinearly on the movable platform at the two sides of the patient's head. Determining the lines of flight of the back-to-back propagating photons enabled reconstruction of the image of ^{74}As concentration in the brain, thus revealing the location of the tumour. This pioneering positron imaging led to the development of positron emission tomography (PET)[221], which is now routinely used in clinical practice, enabling the recognition of tissue abnormalities at the molecular level, before they lead to morphological changes[222]. The effective radiation dose from a PET scan is modest and actually lower than from the more frequently used computed tomography scans.

PET diagnostics has experienced continuous improvements in radiation detection and radiopharmacy, leading to the possibility of dynamic and simultaneous imaging of all patient tissues. This was demonstrated with the total-body PET system constructed from 564,480 crystal scintillators[223]. However, the main principles of PET scanners (recording electron–positron annihilation into two photons), based on localizing the accumulation of pharmaceuticals, have remained unchanged for over 70 years. The recent invention of positronium imaging[224] brought a qualitative breakthrough, enabling the imaging of parameters characterizing the mechanism of positron–electron annihilation in living organisms[225]. These parameters include the mean *ortho*-positronium lifetime (τ_{oPs}) and its formation probability (P_{oPs}), as well as the mean lifetime of positrons undergoing direct annihilation (τ_d), the mean positron lifetime in the tissue (τ_{e+}), the 3γ to 2γ positron annihilation rate ratio ($R_{3/2}$)[226] and the degree of quantum entanglement of annihilation photons (R_{QE})[227,228]. These parameters are sensitive to the molecular environment in which positronium annihilation occurs. In particular, the rate of the pick-off processes depends on the intramolecular arrangement, and the rate of the conversion processes depends on the presence of paramagnetic molecules such as oxygen ($o\text{-}Ps + O_2 \rightarrow p\text{-}Ps + O_2 \rightarrow 2\gamma + O_2$)[229,230]. Consequently, generating images of positronium properties within a living organism, specifically by using τ_{oPs}, τ_{e+}, τ_d, $R_{3/2}$, P_{oPs} and R_{QE}, could reveal early-stage tissue pathology related to molecular changes. These changes precede functional and morphological symptoms[231,232], and their monitoring could be used for non-invasive assessment of the degree of hypoxia[233,234], which is an indicator characterizing the oxygen deficit used to guide the choice of personalized treatment[235].

Glossary

β^+ decay
A form of radioactivity where an unstable isotope decays through the emission of a positron and a neutrino.

Bloch-like state
In a perfect crystalline lattice, the thermalized positron is in a delocalized state dictated by the periodicity of the lattice, described by Bloch wave function.

Coincidence Doppler broadening
(CDB). Doppler broadening measured with two detectors in coincidence, allowing for reduced background noise to a negligible level.

Doppler broadening
Broadening of the 511 keV positron–electron annihilation line in the energy spectrum, caused by the distribution of momenta of the annihilated electrons.

Fast scintillation detectors
A material that emits visible (or ultraviolet/infrared) photons upon irradiation with high-energy photons, typically connected to a photomultiplier tube for electronic signal generation.

High-purity germanium detectors
Semiconductor detectors for high-energy photon detection with high-energy resolution, based on ultrapure germanium, and require cooling to liquid nitrogen temperature.

Implantation depth
The depth at which positrons are implanted in a slow positron beam experiment, often is reported as the mean implantation depth as the implantation profile is very wide at higher energies.

Implantation energy
Kinetic energy of the positrons in a slow positron beam experiment. The probing depth of positrons can be controlled by tuning the implantation energy.

Lifetime
The inverse of the annihilation rate that characterizes the exponential decay process of a positron.

Open volume defects
Atomic-scale defects with excess empty volume. For example, one or several missing atoms in a crystal lattice known as vacant lattice sites or vacancy defects.

Pair production
Spontaneous formation of positron–electron pairs from high-energy γ-radiation.

Positronium
Hydrogen-like bound state of a positron and an electron.

Slow positron beam
A set-up where the positron kinetic energy can be controlled, typically in the range 0–50 keV. Also known as a variable-energy positron beam.

Positronium imaging is rapidly developing[226]. In 2021, the first 3γ-image[236] and τ_{oPs}-image[237] were demonstrated with the dedicated mutiphoton J-PET scanner (where J stands for Jagiellonian University)[238,239] that enables simultaneous registration of two and three annihilation photons as well as prompt γ-rays emitted by radionuclides such as ^{44}Sc (Fig. 6a). ^{44}Sc emits a prompt γ-ray after each positron emission (so that the decay chain is $^{44}Sc \rightarrow {}^{44}Ca^* + e^+ + \nu \rightarrow {}^{44}Ca + \gamma + e^+ + \nu$, where ν is a neutrino) with a mean de-excitation time of only 2.6 ps and is therefore the most promising radionuclide for efficient positronium imaging[240,241]. The annihilation and prompt photons are distinguished based on the energy deposited in scintillators[242]. The registration of prompt γ is used to determine the time when positron is emitted to the body and the registration of annihilation photons is used to reconstruct the time and place of the positron annihilation[243,244].

Positronium imaging research has primarily concentrated on imaging the mean *ortho*-positronium lifetime[234,237,242,245–247], and the development of the reconstruction algorithms that would enable positronium imaging with a few millimetre spatial resolution[248–253]. In 2024, a major step towards translating positronium lifetime imaging into clinical practice was reached with the successful demonstration of the first clinical positronium lifetime images of the human brain[242]. These first in vivo images of the τ_{oPs} values in the brain are shown in Fig. 6. The determined values of τ_{oPs} and τ_{e+} in a glioma tumour are smaller than those in salivary glands, which in turn are smaller than those in healthy brain tissues[242]. In vivo observation of differences in positron and positronium lifetimes between healthy and cancer tissues opens promising perspectives for application of positronium imaging in medical practice. At the time of this publication, there are six PET systems that are capable of measuring the lifetime of positronium: the J-PET scanner in Poland[242], the Prism-PET[252], the PennPET Explorer[246], the NeuroEXPLORER (NX) brain PET in the USA[254], the Biograph Vision Quadra in Switzerland[245] and the brain-dedicated ToF-PET scanner VRAIN in Japan[234]. So far these scanners were used to demonstrate the possibilities of positronium imaging using radionuclides including ^{124}I, ^{82}Rb, ^{68}Ga, ^{55}Co, ^{52}Mn and ^{44}Sc (refs. 242,245,247,255–258).

The future of PAS

PAS is a set of methods that excel in identifying and quantifying material structures with excess open volume, from vacancy defects in crystalline solids such as semiconductors to porosity in disordered media. The most promising advances of the methods allow extending the analysis to materials systems with complex atomic structures, to surfaces and to interfaces. The development of theoretical tools alongside novel experiments offers exciting opportunities for detailed interpretation of the physical processes, while the emergence of positronium imaging in biological systems widens the application horizons of positron annihilation.

Published online: 13 August 2026

References

1. Dirac, P. A. M. The quantum theory of the electron. *Proc. R. Soc. A* **117**, 610–624 (1928).
2. Dirac, P. A. M. A theory of electrons and protons. *Proc. R. Soc. A* **126**, 360–365 (1930).
3. Oppenheimer, J. R. Note on the theory of the interaction of field and matter. *Phys. Rev.* **35**, 461–477 (1930).
4. Dirac, P. A. M. Quantised singularities in the electromagnetic field. *Proc. R. Soc. A* **133**, 60–72 (1931).
5. Anderson, C. D. The apparent existence of easily deflectable positives. *Science* **76**, 238–239 (1932).
6. Anderson, C. D. The positive electron. *Phys. Rev.* **43**, 491–494 (1933).
7. Beringer, R. & Montgomery, C. G. The angular distribution of positron annihilation radiation. *Phys. Rev.* **61**, 222–224 (1942).
8. DeBenedetti, S., Cowan, C. E., Konneker, W. R. & Primakoff, H. On the angular distribution of two-photon annihilation radiation. *Phys. Rev.* **77**, 205–212 (1949).
9. Shearer, J. W. & Deutsch, M. The lifetime of positrons in matter. *Phys. Rev.* **76**, 462 (1949).
10. Hanna, S. S. & Preston, R. S. Positron polarization demonstrated by annihilation in magnetized iron. *Phys. Rev.* **106**, 1363–1364 (1957).
11. Berko, S. & Hereford, F. L. Experimental studies of positron interactions in solids and liquids. *Rev. Mod. Phys.* **28**, 299–307 (1956).
12. Ferrell, R. A. Theory of positron annihilation in solids. *Rev. Mod. Phys.* **28**, 308–337 (1956).
13. West, R. N. *Positron Studies of Condensed Matter* (Taylor & Francis, 1974).
14. Asoka-Kumar, P., Lynn, K. G. & Welch, D. O. Characterization of defects in Si and SiO_2–Si using positrons. *J. Appl. Phys.* **76**, 4935–4982 (1994).
15. Puska, M. J. & Nieminen, R. M. Theory of positrons in solids and on solid surfaces. *Rev. Mod. Phys.* **66**, 841–897 (1994).
16. Saarinen, K., Hautojärvi, P. a& Corbel, C. in *Semiconductors and Semimetals* (ed. Stavola, M.) Vol. 51A 209–285 (Academic Press, 1998).
17. Krause-Rehberg, R. & Leipner, H. S. *Positron Annihilation in Semiconductors: Defect Studies* Vol. 127 (Springer, 1999).
18. Tuomisto, F. & Makkonen, I. "Defect identification in semiconductors with positron annihilation: experiment and theory". *Rev. Mod. Phys.* **85**, 1583–1631 (2013).

19. Cizek, J. Characterization of lattice defects in metallic materials by positron annihilation spectroscopy: a review. *J. Mater. Sci. Technol.* **34**, 577 (2018).
20. Selim, F. A. Positron annihilation spectroscopy of defects in nuclear and irradiated materials- a review. *Mater. Charact.* **174**, 110952 (2021).
21. Makkonen, I. & Tuomisto, F. Perspective on defect characterization in semiconductors by positron annihilation spectroscopy. *J. Appl. Phys.* **135**, 040901 (2024).
22. Schultz, P. J. & Lynn, K. G. Interaction of positron beams with surfaces, thin films, and interfaces. *Rev. Mod. Phys.* **60**, 801–779 (1988).
23. Jean, Y. C., Mallon, P. E. & Schrader, D. M. (eds) *Principles and Applications of Positron and Positronium Chemistry* (World Scientific, 2003).
24. Becvar, F. et al. A high-resolution BaF_2 positron-lifetime spectrometer and experience with its long-term exploitation. *Nucl. Instr. Meth. Phys. Res. A* **443**, 557–577 (2000).
25. Djourelov, N. & Misheva, M. Source correction in positron annihilation lifetime spectroscopy. *J. Phys. Condens. Matter* **8**, 2081–2087 (1996).
26. van Veen, A. et al. Intense positron souces and their applications. *Mater. Sci. Forum* **363–365**, 415–419 (2001).
27. Wagner, A., Butterling, M., Liedke, M. O., Potzger, K. & Krause-Rehberg, R. Positron annihilation lifetime and doppler broadening spectroscopy at the ELBE Facility. *AIP Conf. Proc.* **1970**, 040003 (2018).
28. Hugenschmidt, C. Positrons in surface physics. *Surf. Sci. Rep.* **71**, 547–594 (2016).
29. Weiss, A. et al. Auger-electron emission resulting from the annihilation of core electrons with low-energy positrons. *Phys. Rev. Lett.* **61**, 2245–2248 (1988).
30. Weiss, A., Mehl, D., Koymen, A. R., Lee, K. H. & Lei, C. Elimination of the secondary electron background in auger electron spectroscopy using low energy positron excitation. *J. Vac. Sci. Technol. A* **8**, 2517–2520 (1990).
31. Hugenschmidt, C., Mayer, J. & Schreckenbach, K. Surface investigation of Si(100), Cu, Cu on Si(100), and Au on Cu with positron annihilation induced Auger-electron spectroscopy. *Surf. Sci.* **601**, 2459–2466 (2007).
32. Asoka-Kumar, P. et al. Increased elemental specificity of positron annihilation spectra. *Phys. Rev. Lett.* **77**, 2097–2100 (1996).
33. Peng, J. P., Lynn, K. G., Asoka-Kumar, P., Becker, D. P. & Harshman, D. R. Study of the SiO_2–Si interface using variable energy positron two-dimensional angular correlation of annihilation radiation. *Phys. Rev. Lett.* **76**, 2157–2160 (1996).
34. Green, D. G. Probing positron cooling in noble gases via annihilation γ spectra. *Phys. Rev. Lett.* **119**, 203404 (2017).
35. Boroński, E. & Nieminen, R. M. Electron–positron density-functional theory. *Phys. Rev. B* **34**, 3820–3831 (1986).
36. Mäki, J.-M. et al. Time dependence of charge transfer processes in diamond studied with positrons. *Phys. Rev. Lett.* **107**, 217403 (2011).
37. Uedono, A. et al. Effects of ultra-high-pressure annealing on characteristics of vacancies in Mg-implanted GaN studied using a monoenergetic positron beam. *Sci. Rep.* **10**, 17349 (2020).
38. Saarinen, K. et al. Observation of native Ga vacancies in GaN by positron annihilation. *Phys. Rev. Lett.* **79**, 3030–3033 (1997).
39. Rauch, C., Makkonen, I. & Tuomisto, F. Identifying vacancy complexes in compound semiconductors with positron annihilation spectroscopy: a case study of InN. *Phys. Rev. B* **84**, 125201 (2011).
40. Mäki, J.-M. et al. Identification of the V_{Al}–O_N defect complex in AlN single crystals. *Phys. Rev. B* **84**, 081204 (2011).
41. Prozheev, I., Heikkinen, T., Makkonen, I., Mizohata, K. & Tuomisto, F. In-grown and irradiation-induced Al and N vacancies in 100 keV H^+ implanted AlN single crystals. *Jpn J. Appl. Phys.* **63**, 071001 (2024).
42. Uedono, A. et al. Effect of ultra-high-pressure annealing on defect reactions in ion-implanted GaN studied by positron annihilation. *Phys. Status Solidi B* **259**, 2200183 (2022).
43. Sakurai, H. et al. Highly effective activation of Mg-implanted p-type GaN by ultra-high-pressure annealing. *Appl. Phys. Lett.* **115**, 142104 (2019).
44. Narita, T., Uedono, A. & Kachi, T. Effects of hydrogen incorporation on Mg diffusion in GaN-doped with Mg ions via ultra-high-pressure annealing. *Phys. Status Solidi B* **259**, 2200235 (2022).
45. Chichibu, S. F. et al. Origin of defect-insensitive emission probability in In-containing (Al,In,Ga)N alloy semiconductors. *Nat. Mater.* **5**, 810–816 (2006).
46. Prozheev, I., Mehnke, F., Wernicke, T., Kneissl, M. & Tuomisto, F. Electrical compensation and cation vacancies in Al rich Si-doped AlGaN. *Appl. Phys. Lett.* **117**, 142103 (2020).
47. Prozheeva, V. et al. Interfacial N vacancies in GaN/(Al,Ga)N/GaN heterostructures. *Phys. Rev. Appl.* **13**, 044034 (2020).
48. Uedono, A. et al. Vacancy-type defects in AlInN/AlN/GaN structures probed by monoenergetic positron beam. *J. Appl. Phys.* **133**, 225301 (2023).
49. Prozheev, I. et al. Short-range order controlled amphoteric behavior of the Si dopant in Al-rich AlGaN. *Nat. Commun.* **16**, 5005 (2025).
50. van Veen, A. et al. VEPFIT applied to depth profiling problems. *Appl. Surf. Sci.* **85**, 216 (1995).
51. Seeger, A. Investigation of point defects in equilibrium concentrations with particular reference to positron annihilation techniques. *J. Phys. F* **3**, 248–294 (1973).
52. Fluss, M. J., Smedskjaer, L. C., Chason, M. K., Legnini, D. G. & Siegel, R. W. Measurements of the vacancy formation enthalpy in aluminum using positron annihilation spectroscopy. *Phys. Rev. B* **17**, 3444 (1978).
53. Schaefer, H.-E. et al. Thermal vacancies and positron-lifetime measurements in $Fe_{76.3}Al_{23.7}$. *Phys. Rev. B* **41**, 11869 (1990).
54. Würschum, R., Grupp, C. & Schaefer, H.-E. Simultaneous study of vacancy formation and migration at high temperatures in B2-type fe aluminides. *Phys. Rev. Lett.* **75**, 97 (1995).
55. Elsayed, M., Staab, T. E. M., Cizek, J. & Krause-Rehberg, R. Monovacancy–hydrogen interaction in pure aluminum: experimental and ab-initio theoretical positron annihilation study. *Acta Mater.* **248**, 118770 (2023).
56. Haraguchi, T., Hori, F., Oshima, R. & Kogachi, M. A study of vacancy-type defects in the B2-phase region of the Fe–Al system by positron annihilation method. *Intermetallics* **9**, 763 (2001).
57. Golovin, I. S., Divinski, S. V., Čížek, J., Procházka, I. & Stein, F. Study of atom diffusivity and related relaxation phenomena in Fe_3Al–(Ti,Nb)–C alloys. *Acta Mater.* **53**, 2581 (2005).
58. Hautojärvi, P., Johansson, J., Vehanen, A., Yli-Kauppila, J. & Moser, P. Vacancy–carbon interaction in iron. *Phys. Rev. Lett.* **44**, 1326 (1980).
59. Vehanen, A., Hautojärvi, P., Johansson, J., Yli-Kauppila, J. & Moser, P. Vacancies and carbon impurities in α-iron: electron irradiation. *Phys. Rev. B* **25**, 762 (1982).
60. Cizek, J. et al. Hydrogen–vacancy complexes in electron-irradiated niobium. *Phys. Rev. B* **79**, 054108 (2009).
61. Ogorodnikova, O. V. et al. Verification of the theory of primary radiation damage by comparison with experimental data. *J. Nucl. Mater.* **525**, 22 (2019).
62. Cizek, J. et al. The development of vacancies during severe plastic deformation. *Mater. Trans.* **60**, 1533 (2019).
63. Cizek, J. et al. Characterizing deformation by positron annihilation spectroscopy: cold spray versus high-pressure torsion. *J. Therm. Spray Tech.* **34**, 2710 (2025).
64. Puska, M. J. & Nieminen, R. M. Defect spectroscopy with positrons: a general calculational method. *J. Phys. F* **13**, 333 (1983).
65. Kuramoto, E., Tsutsumi, T., Ueno, K., Ohmura, M. & Kamimura, Y. Positron lifetime calculations on vacancy clusters and dislocations in Ni and Fe. *Comput. Mater. Sci.* **14**, 28 (1999).
66. Fukai, Y. & Ōkuma, N. Formation of superabundant vacancies in Pd hydride under high hydrogen pressures. *Phys. Rev. Lett.* **73**, 1640 (1994).
67. Shirai, Y., Araki, H., Mori, T., Nakamura, W. & Sakaki, K. Positron annihilation study of lattice defects induced by hydrogen absorption in some hydrogen storage materials. *J. Alloy Compd* **330**, 125 (2002).
68. Cizek, J. et al. Hydrogen-induced defects in bulk niobium. *Phys. Rev. B* **69**, 224106 (2004).
69. Elsayed, M., Staab, T. E. M., Cizek, J. & Krause-Rehberg, R. On the interaction of solute atoms with vacancies in diluted Al-alloys: a paradigmatic experimental and ab-initio study on indium and tin. *Acta Mater.* **219**, 117228 (2021).
70. Pogatscher, S. et al. Diffusion on demand to control precipitation aging: application to Al–Mg–Si alloys. *Phys. Rev. Lett.* **112**, 225701 (2014).
71. Somoza, A. & Dupasquier, A. Positron studies of solute aggregation in age-hardenable aluminum alloys. *J. Mater. Proc. Technol.* **135**, 83 (2003).
72. Zivotsky, O. et al. Microstructural and magnetic properties of Mn_2FeSi and Mn_2FeAl alloys prepared in bulk form. *J. Alloy Compd* **947**, 169672 (2023).
73. Cizek, J., Lukac, F., Melikhova, O., Prochazka, I. & Kuzel, R. Thermal vacancies in Fe_3Al studied by positron annihilation. *Acta Mater.* **59**, 4068 (2011).
74. Smedskjaer, L. C., Manninen, M. & Fluss, M. J. An alternative interpretation of positron annihilation in dislocations. *J. Phys. F Met. Phys.* **10**, 2237 (1980).
75. Janecek, J. C. M. et al. Evolution of defects in copper deformed by high-pressure torsion. *Acta Mater.* **59**, 2322–2329 (2011).
76. Janecek, J. C. M. et al. Structural characterization of ultrafine-grained interstitial-free steel prepared by severe plastic deformation. *Acta Mater.* **105**, 258–272 (2016).
77. Puska, M. J., Lanki, P. & Nieminen, R. M. Positron affinities for elemental metals. *J. Phys. Condens. Matter* **1**, 6081–6094 (1989).
78. Nagai, Y. et al. Positron confinement in ultrafine embedded particles: quantum-dot-like state in an Fe–Cu alloy. *Phys. Rev. B* **61**, 6574–6578 (2000).
79. Vlach, M. et al. Phase transformations in novel hot-deformed Al–Zn–Mg–Cu–Si–Mn–Fe(–Sc–Zr) alloys. *Mater. Des.* **193**, 108821 (2020).
80. Procházka, I. et al. Positron annihilation study of yttria-stabilized zirconia nanopowders containing Cr_2O_3 additive. *J. Phys. Conf. Ser.* **265**, 012020 (2011).
81. Cao, S. et al. Exploration about superior anti-counterfeiting ability of Sm^{3+} doped $KSr_2Nb_5O_{15}$ photochromic ceramics: origin and atomic-scale mechanism. *J. Materiomics* **8**, 38–46 (2022).
82. Reiner, M., Gigl, T., Jany, R., Hammerl, G. & Hugenschmidt, C. Detection and imaging of the oxygen deficiency in single crystalline $YBa_2Cu_3O_7$–δthin films using a scanning positron beam. *Appl. Phys. Lett.* **106**, 111910 (2015).
83. Reiner, M., Gigl, T., Jany, R., Hammerl, G. & Hugenschmidt, C. Impact of oxygen diffusion on superconductivity in$YBa_2Cu_3O_7$–δthin films studied by positron annihilation spectroscopy. *Phys. Rev. B* **97**, 144503 (2018).
84. Qin, M. et al. Point defect structure of La-doped $SrTiO_3$ ceramics with colossal permittivity. *Acta Mater.* **164**, 76–89 (2019).
85. Evans, E. H., Evans, J. H., Rice-Evans, P., Smith, D. L. & Smith, C. A slow positron study into the recovery behaviour of as-polished and krypton-implanted uranium dioxide. *J. Nucl. Mater.* **199**, 79–83 (1992).
86. Wiktor, J. et al. Coupled experimental and DFT plus U investigation of positron lifetimes in UO_2. *Phys. Rev. B* **90**, 184101 (2014).
87. Barthe, M.-F. et al. Positron annihilation characteristics in UO_2: for lattice and vacancy defects induced by electron irradiation. *Phys. Status Solidi* **4**, 3627–3632 (2007).

88. Wiktor, J., Jomard, G., Torrent, M. & Bertolus, M. First-principles calculations of momentum distributions of annihilating electron–positron pairs in defects in UO_2. *J. Phys. Condens. Matter* **29**, 035503 (2017).
89. Vitkovska, E. Okal, M. & Ballo, P. Simulation of positron lifetimes in uranium dioxide: an ab initio study. In *Proc. 21 International Conference on Applied Physics of Condensed Matter and of the Scientific Conference Advanced Fast Reactors* INIS-SK--2018-012, 29 (International Atomic Energy Agency, 2015).
90. Mackenzie, I. K., Khoo, T. L., McDonald, A. B. & McKee, B. T. A. Temperature dependence of positron mean lives in metals. *Phys. Rev. Lett.* **19**, 946–948 (1967).
91. Cotterill, R., MacKenzie, I. K., Smedskjaer, L., Trumpy, G. & Träff, J. Correlation of void size and positron annihilation characteristics in neutron-irradiated molybdenum. *Nature* **239**, 99 (1972).
92. Triftshäuser, W., McGervey, J. D. & Hendricks, R. W. Positron-annihilation studies of voids in neutron-irradiated aluminum single crystals. *Phys. Rev. B* **9**, 3321 (1974).
93. Selim, F. A. et al. Radiation-induced vacancy injection in heterogeneous multiphase materials. *Cell Rep. Phys. Sci.* **6**, 102989 (2025).
94. Eldrup, M. & Singh, B. N. Study of defect annealing behaviour in neutron irradiated Cu and Fe using positron annihilation and electrical conductivity. *J. Nucl. Mater.* **276**, 269 (2000).
95. Iwai, T., Ito, Y. & Koshimizu, M. Vacancy-type defect production in iron under ion beam irradiation investigated with positron beam Doppler broadening technique. *J. Nucl. Mater.* **329**, 963 (2004).
96. Lambrecht, M. & Malerba, L. Positron annihilation spectroscopy on binary Fe–Cr alloys and ferritic/martensitic steels after neutron irradiation. *Acta Mater.* **59**, 6547 (2011).
97. Sato, K. et al. Positron annihilation spectroscopy of ferritic/martensitic steels F82H and T91 irradiated with protons and neutrons at PSI. *J. Nucl. Mater.* **450**, 59 (2014).
98. Triftshäuser, W. & Kögel, G. Defect structures below the surface in metals investigated by monoenergetic positrons. *Phys. Rev. Lett.* **48**, 1741 (1982).
99. Lynn, K. G., Chen, D. M., Nielsen, B., Pareja, R. & Myers, S. Variable-energy positron-beam studies of Ni implanted with He. *Phys. Rev. B* **34**, 1449 (1986).
100. Sato, K. et al. Positron annihilation lifetime measurements of He-ion-irradiated Fe using pulsed positron beam. *J. Phys. Conf. Ser.* **262**, 012053 (2011).
101. Iwai, T. & Tsuchida, H. In situ positron beam Doppler broadening measurement of ion-irradiated metals — current status and potential. *Nucl. Instrum. Methods Phys. Res. B* **285**, 18 (2012).
102. Uedono, A. et al. Annealing properties of vacancy-type defects in ion-implanted GaN studied by monoenergetic positron beams. *J. Appl. Phys.* **102**, 084505 (2007).
103. Tuomisto, F., Saarinen, K., Look, D. C. & Farlow, G. C. Introduction and recovery of point defects in electron-irradiated ZnO. *Phys. Rev. B* **72**, 085206 (2005).
104. Tuomisto, F. et al. Segregation of Ni at early stages of radiation damage in NiCoFeCr solid solution alloys. *Acta Mater.* **196**, 44 (2020).
105. Agarwal, S. et al. A new mechanism for void-cascade interaction from nondestructive depth-resolved atomic-scale measurements of ion irradiation-induced defects in Fe. *Sci. Adv.* **6**, eaba8437 (2020).
106. Seyedrezai, H., Grebennikov, D., Mascher, P. & Zurob, H. S. Study of the early stages of clustering in Al–Mg–Si alloys using the electrical resistivity measurements. *Mater. Sci. Eng. A* **525**, 186 (2009).
107. Nagai, Y., Tang, Z., Hasegawa, M., Kanai, T. & Saneyasu, M. Irradiation-induced Cu aggregations in Fe: an origin of embrittlement of reactor pressure vessel steels. *Phys. Rev. B* **63**, 134110 (2001).
108. Nagai, Y. et al. Positron confinement in ultrafine embedded particles: quantum-dot-like state in an Fe–Cu alloy. *Phys. Rev. B* **61**, 6574 (2000).
109. Auguste, R. et al. In situ measurements of non-equilibrium positron state defects during He irradiation in Si. *J. Appl. Phys.* **133**, 185901 (2023).
110. Lee, T. D. & Yang, C. N. Question of parity conservation in weak interactions. *Phys. Rev.* **104**, 254–258 (1956).
111. Berko, S. & Zuckerman, J. Polarized positron annihilation in ferromagnets. *Phys. Rev. Lett.* **13**, 399–341 (1964).
112. Mijnarends, P. E. & Hambro, L. Positron annihilation in magnetised single crystals of iron. *Phys. Lett.* **10**, 272–273 (1964).
113. Zitzewitz, P. W., Van House, J. C., Rich, A. & Gidley, D. W. Spin polarization of low-energy positron beams. *Phys. Rev. Lett.* **43**, 1281–1284 (1979).
114. Kawasuso, A. Spin-polarized positron annihilation spectroscopy: principles and applications in materials study. *Solid. State Phenom.* **373**, 39–48 (2025).
115. Kawasuso, A., Maekawa, M., Fukaya, Y., Yabuuchi, A. & Mochizuki, I. Spin-polarized positron annihilation measurements of polycrystalline Fe, Co, Ni, and Gd based on Doppler broadening of annihilation radiation. *Phys. Rev. B* **83**, 100406 (2011).
116. Kawasuso, A., Maekawa, M., Fukaya, Y., Yabuuchi, A. & Mochizuki, I. Doppler broadening of annihilation radiation measurements on 3*d* and 4*f* ferromagnets using polarized positrons. *Phys. Rev. B* **85**, 024417 (2012).
117. Weber, J. A. et al. Spin-resolved fermi surface of the localized ferromagnetic heusler compound Cu_2MnAl measured with spin-polarized positron annihilation. *Phys. Rev. Lett.* **115**, 206404 (2015).
118. Hanssen, K. E. H. M., Mijnarends, P. E., Rabou, L. P. L. M. & Buschow, K. H. J. Positron-annihilation study of the half-metallic ferromagnet NiMnSb: experiment. *Phys. Rev. B* **42**, 1533–1540 (1990).
119. Maekawa, M. et al. Vacancy-induced ferromagnetism in ZnO probed by spin-polarized positron annihilation spectroscopy. *Appl. Phys. Lett.* **110**, 172402 (2017).
120. Maekawa, M., Miyashita, A., Sakai, S. & Kawasuso, A. Gadolinium-implanted GaN studied by spin-polarized positron annihilation spectroscopy. *Phys. Rev. B* **102**, 054427 (2020).
121. Kawasuso, A. et al. Electron spins at surface, interface and vacancy detected by spin-polarized positron annihilation spectroscopy. *J. Phys. Conf. Ser.* **3029**, 012021 (2025).
122. Gidley, D. W., Koymen, A. R. & Capehart, T. W. Polarized low-energy positrons: a new probe of surface magnetism. *Phys. Rev. Lett.* **49**, 1779–1783 (1982).
123. Kawasuso, A. et al. Current-induced spin polarization on a Pt surface: a new approach using spin-polarized positron annihilation spectroscopy. *J. Mag. Mag. Mater.* **342**, 139–143 (2013).
124. Zhang, H. J. et al. Current-induced spin polarization on metal surfaces probed by spin-polarized positron beam. *Sci. Rep.* **4**, 04844 (2014).
125. Zhang, H. J. et al. Charge-to-spin conversion and spin diffusion in Bi/Ag bilayers observed by spin-polarized positron beam. *Phys. Rev. Lett.* **114**, 166602 (2015).
126. Miyashita, A. et al. Spin polarization of graphene and *h*–BN on Co(0001) and Ni(111) observed by spin-polarized surface positronium spectroscopy. *Phys. Rev. B* **97**, 195405 (2018).
127. Miyashita, A., Li, S., Sakai, S., Maekawa, M. & Kawasuso, A. Spin polarization of graphene on $Co_2FeGe_{0.5}Ga_{0.5}$ (001) observed by spin-polarized surface positronium spectroscopy. *Phys, Rev. B* **102**, 045425 (2020).
128. Gilbert, S. J. & Dowben, P. A. Direct measurements of proximity induced spin polarization in 2D systems. *J. Phys. D* **53**, 343001 (2020).
129. Maekawa, M. et al. Spin-polarized positronium time-of-flight spectroscopy for probing spin-polarized surface electronic states. *Phys. Rev. Lett.* **126**, 186401 (2021).
130. Kawasuso, A. & Maekawa, M. Spin-polarized surface positronium spectroscopy — current status and future. *Acta Phys. Polonica B* **17**, 1-A4 (2024).
131. Keeble, D. J. et al. Identification of A- and B-site cation vacancy defects in perovskite oxide thin films. *Phys. Rev. Lett.* **105**, 226102 (2010).
132. Karjalainen, A. et al. Ti_{Sr} antisite: an abundant defect in $SrTiO_3$. *J. Appl. Phys.* **127**, 245702 (2020).
133. Keeble, D. J. et al. Identification of lead vacancy defects in lead halide perovskites. *Nat. Commun.* **12**, 5566 (2021).
134. Musiienko, A. et al. Origin of defects and positron annihilation in hybrid and all-inorganic perovskites. *Chem. Mater.* **34**, 297 (2022).
135. Ni, Z. et al. Identification and suppression of point defects in bromide perovskite single crystals enabling gamma-ray spectroscopy. *Adv. Mater.* **36**, 2406193 (2024).
136. Ni, X. et al. Effect of Br content on phase stability and performance of $H_2N{=}CHNH_2Pb(I_{1-x}Br_x)_3$ perovskite thin films. *Nanotechnology* **30**, 165402 (2019).
137. Koushik, D. et al. On the effect of atomic layer deposited Al_2O_3 on the environmental degradation of hybrid perovskite probed by positron annihilation spectroscopy. *J. Mater. Chem. C* **7**, 5275 (2019).
138. Schmidt, J. A. et al. Positron annihilation lifetime spectroscopy of single crystalline $CH_3NH_3PbBr_3$: experiments and ab initio calculations. *J. Phys. Chem. C* **129**, 7207 (2025).
139. Madaan, K. et al. Challenges in predicting positron annihilation lifetimes in lead halide perovskites: correlation functionals and polymorphism. *Phys. Rev. B* **113**, 184118 (2026).
140. Zhang, X. et al. A historical overview of the activation and porosity of metal–organic frameworks. *Chem. Soc. Rev.* **49**, 7406 (2020).
141. Zaleski, R. Principles of positron porosimetry. *Nukleonika* **60**, 795 (2015).
142. Mondal, S. S. et al. Study of the discrepancies between crystallographic porosity and guest access into cadmium–imidazolate frameworks and tunable luminescence properties by incorporation of lanthanides. *Chem. A Eur. J.* **22**, 6905 (2016).
143. Feldblyum, J. I. et al. Reconciling the discrepancies between crystallographic porosity and guest access as exemplified by Zn-HKUST-1. *J. Am. Chem. Soc.* **133**, 18257 (2011).
144. Thornton, A. W. et al. Porosity in metal–organic framework glasses. *Chem. Commun.* **52**, 3750 (2016).
145. Liu, M. et al. Evolution of nanoscale pore structure in coordination polymers during thermal and chemical exposure revealed by positron annihilation. *Adv. Mater.* **22**, 1598 (2010).
146. Attallah, A. G. et al. Uncovering the dynamic CO_2 Gas uptake behavior of CALF-20 (Zn) under varying conditions via positronium lifetime analysis. *Small* **21**, 2500544 (2025).
147. Attallah, A. G. et al. Revisiting metal–organic frameworks porosimetry by positron annihilation: metal ion states and positronium parameters. *J. Phys. Chem. Lett.* **15**, 4560 (2024).
148. Dutta, D. et al. Evidence of positronium bloch states in porous crystals of Zn_4O-coordination polymers. *Phys. Rev. Lett.* **110**, 197403 (2013).
149. Stassin, T. R. et al. Porosimetry for thin films of metal–organic frameworks: a comparison of positron annihilation lifetime spectroscopy and adsorption-based methods. *Adv. Mater.* **33**, 2006993 (2021).
150. Duke, M. C. et al. Structural effects on SAPO-34 and ZIF-8 materials exposed to seawater solutions, and their potential as desalination membranes. *Desalination* **377**, 128 (2016).
151. Zhang, X. et al. Dependence of dye molecules adsorption behaviors on pore characteristics of mesostructured MOFs fabricated by surfactant template. *ACS Appl. Mater. Interfaces* **11**, 31441 (2019).
152. Sharma, S. K. et al. Crystal size-dependent pore architecture and surface chemical characteristics of desolvated ZIF-8 investigated using positron annihilation spectroscopy. *J. Phys. Chem. C.* **124**, 25291 (2020).
153. Attallah, A. G. et al. Unravelling the water adsorption mechanism in hierarchical MOFs: insights from in situ positron annihilation lifetime studies. *ACS Appl. Mater. Interfaces* **15**, 48264 (2023).
154. Shukla, A., Hoffmann, L., Manuel, A. A. & Peter, M. Melt 4.0 a program for positron lifetime analysis. *Mater. Sci. Forum* **255–257**, 233 (1997).
155. Zaleski, R. Measurement and analysis of the positron annihilation lifetime spectra for mesoporous silica. *Acta Phys. Polonica A* **110**, 729 (2006).

156. Tao, S. J. Positronium annihilation in molecular substances. *J. Chem. Phys.* **56**, 5499–5510 (1972).
157. Eldrup, M., Lightbody, D. & Sherwood, J. N. The temperature dependence of positron lifetimes in solid pivalic acid. *Chem. Phys.* **63**, 51–58 (1981).
158. Goworek, T., Ciesielski, K., Jasinska, B. & Wawryszczuk, J. Positronium in large voids. Silicagel. *Chem. Phys. Lett.* **272**, 91–95 (1997).
159. Dull, T. L. et al. Determination of pore size in mesoporous thin films from the annihilation lifetime of positronium. *J. Phys. Chem. B* **105**, 4657–4662 (2001).
160. Kuncewicz, J. The extended Tao–Eldrup model. *Marie Curie-Sklodowska University* http://positron.umcs.pl/model/ (accessed 30 October 2025).
161. Gorgol, M., Tydda, M., Kierys, A. & Zaleski, R. Composition of pore surface investigated by positron annihilation lifetime spectroscopy. *Microporous Mesoporous Mater.* **163**, 276–281 (2012).
162. Wada, K. & Hyodo, T. A simple shape-free model for pore-size estimation with positron annihilation lifetime spectroscopy. *J. Phys. Conf. Ser.* **443**, 012003 (2013).
163. Zaleski, R., Błażewicz, A. & Kierys, A. *Ortho*-positronium migration in mesopores of MCM-41, MSF and SBA-3. *Nukleonika* **58**, 233 (2013).
164. Warringham, R. et al. Insights into the mechanism of zeolite detemplation by positron annihilation lifetime spectroscopy. *J. Phys. Chem. C.* **120**, 25451–25461 (2016).
165. Koymen, A. R. et al. Temperature-dependent top-layer composition of ultrathin Pd films on Cu (100). *Phys. Rev. B* **48**, 2020–2023 (1993).
166. Mehl, D. et al. Sensitivity of positron-annihilation-induced Auger-electron spectroscopy to the top surface layer. *Phys. Rev. B* **41**, 799–802 (1990).
167. Yang, G., Kim, J. H., Yang, S. & Weiss, A. H. Adsorption site identification for oxygen molecules on AuSi (100) by positron annihilation induced Auger electron spectroscopy (PAES). *Appl. Surf. Sci.* **85**, 77–81 (1995).
168. Nadesalingam, M. P. et al. Effect of vacuum annealing on the surface chemistry of electrodeposited copper (I) oxide layers as probed by positron annihilation induced Auger electron spectroscopy. *Langmuir* **23**, 1830–1834 (2007).
169. Mayer, J., Hugenschmidt, C. & Schreckenbach, K. Direct observation of the surface segregation of Cu in Pd by time-resolved positron-annihilation-induced Auger electron spectroscopy. *Phys. Rev. Lett.* **105**, 207401 (2010).
170. Mayer, J., Hugenschmidt, C. & Schreckenbach, K. High resolution positron annihilation induced Auger electron spectroscopy of the CuM2,3VV-transition and of Cu sub-monolayers on Pd and Fe. *Surf. Sci.* **604**, 1772–1777 (2010).
171. Chirayath, V. A. et al. Auger electron emission initiated by the creation of valence-band holes in graphene by positron annihilation. *Nat. Commun.* **8**, 16116 (2017).
172. Fairchild, A. J. et al. Direct evidence for low-energy electron emission following O LVV Auger transitions at oxide surfaces. *Sci. Rep.* **10**, 17993 (2020).
173. Eshed, A. et al. Gamma spectra resulting from the annihilation of positrons with electrons in a single core level. *Phys. Rev. Lett.* **89**, 075503 (2002).
174. Kim, S. et al. Gamma-ray spectra resulting from the annihilation of positrons with selected core levels of Cu, Ag, and Au. *Phys. Rev. B* **73**, 014114 (2006).
175. Gladen, R. W. et al. Identification of Auger mechanisms responsible for low energy electron emission from graphene on copper using Auger–gamma coincidence spectroscopy. *J. Electron. Spectrosc. Relat. Phenom.* **251**, 147095 (2021).
176. Lotfimarangloo, S. et al. Measurement and analysis of the Doppler broadened energy spectra of gamma radiation originating from the annihilation of positrons incident on clean and adsorbate-covered surfaces. *Appl. Surf. Sci.* **689**, 162372 (2025).
177. O'Rourke, B. E., Yamawaki, M. & Ito, K. Development of an ISO technical specification for evaluation of pore size in materials via the positron annihilation lifetime technique. *J. Phys. Conf. Ser.* **3029**, 012025 (2025).
178. Linez, F., Makkonen, I. & Tuomisto, F. Calculation of positron annihilation characteristics of six main defects in 6*H*-SiC and the possibility to distinguish them experimentally. *Phys. Rev. B* **94**, 014103 (2016).
179. Tuomisto, F. Identification of point defects in multielement compounds and alloys with positron annihilation spectroscopy: challenges and opportunities. *Phys. Status Solidi Rapid Res. Lett.* **15**, 2100177 (2021).
180. Zhelezova, I., Makkonen, I. & Tuomisto, F. On the nature of as-grown and irradiation-induced Ga vacancy defects in β-Ga_2O_3. *J. Appl. Phys.* **136**, 065702 (2024).
181. Edwardson, C. J., Coleman, P. G., Paez, D. J., Doylend, J. K. & Knights, A. P. Direct observation of electron capture and reemission by the divacancy via charge transient positron spectroscopy. *Phys. Rev. Lett.* **110**, 136401 (2013).
182. Nakajima, M., Kinomura, A., Xu, Q. & Kuriyama, K. Transient positron annihilation spectroscopy under light irradiation at liquid nitrogen temperature: evaluation of defect states in single-crystal ZnO. *Jpn J. Appl. Phys.* **63**, 038005 (2024).
183. Yamawaki, M., Kobayashi, Y., Hattori, K. & Watanabe, Y. Novel system for potential nondestructive material inspection using positron annihilation lifetime spectroscopy. *Japn J. Appl. Phys.* **50**, 086301 (2011).
184. Chen, Y. W. et al. Non-beam-based positron annihilation lifetime and coincidence Doppler broadening joint spectrometer for a single piece of micron-thick film. *Nucl. Instrum. Methods Phys. Res. A* **1080**, 170703 (2025).
185. Hegstrom, R. A. β Decay and the origins of biological chirality: theoretical results. *Nature* **297**, 643–647 (1982).
186. Seeger, A., Major, J. & Banhart, F. The study of positron diffusion in solids by positron spin relaxation (e+SR) experiments. *Phys. Stat. Sol.* **102**, 91–106 (1987).
187. Adkins, G. S., Cassidy, D. B. & Perez-Rios, J. Precision spectroscopy of positronium: testing bound-state QED theory and the search for physics beyond the standard model. *Phys. Rep.* **975**, 1–61 (2022).
188. Newson, D. M. & Cassidy, D. B. Measurement of the spin polarization of a slow positron beam using circularly polarized microwave radiation. *Phys. Rev. Lett.* **133**, 233004 (2024).
189. Simula, K. A., Muff, J. E., Makkonen, I. & Drummond, N. D. Quantum Monte Carlo study of positron lifetimes in solids. *Phys. Rev. Lett.* **129**, 166403 (2022).
190. Simula, K. A. et al. Quantum Monte Carlo study of Doppler broadening of positron annihilation radiation in semiconductors and insulators. *Phys. Rev. B* **108**, 045201 (2023).
191. Hofierka, J., Cunningham, B., Rawlins, C. M., Patterson, C. H. & Green, D. G. Many-body theory of positron binding to polyatomic molecules. *Nature* **606**, 688–693 (2022).
192. Green, D. G. & Gribakin, G. F. γ-Ray spectra and enhancement factors for positron annihilation with core electrons. *Phys. Rev. Lett.* **114**, 093201 (2015).
193. Green, D. G., Ludlow, J. A. & Gribakin, G. F. Positron scattering and annihilation on noble-gas atoms. *Phys. Rev. A* **90**, 032712 (2024).
194. Green, D. G. Positron cooling and annihilation in noble gases. *Phys. Rev. Lett.* **119**, 203403 (2017).
195. Arthur-Baidoo, E. et al. Positron annihilation and binding in aromatic and other ring molecules. *Phys. Rev. A* **109**, 062801 (2024).
196. Green, D. G., Swann, A. R. & Gribakin, G. F. Many-body theory for positronium-atom interactions. *Phys. Rev. Lett.* **120**, 183402 (2018).
197. Swann, A. R., Green, D. G. & Gribakin, G. F. Many-body theory of positronium scattering and pickoff annihilation in noble-gas atoms. *Phys. Rev. A* **107**, 042802 (2023).
198. Lavroff, R. H. et al. Aperiodic defects in periodic solids. *J. Chem. Phys.* **163**, 084105 (2025).
199. Puska, M. J., Corbel, C. & Nieminen, R. M. Positron trapping in semiconductors. *Phys. Rev. B* **41**, 9980 (1990).
200. Zhao, F., Turiansky, M. E., Alkauskas, A. & Van de Walle, C. G. Trap-assisted Auger–Meitner recombination from first principles. *Phys. Rev. Lett.* **131**, 056402 (2023).
201. Alkauskas, A., Yan, Q. & Van de Walle, C. G. First-principles theory of nonradiative carrier capture via multiphonon emission. *Phys. Rev. B* **90**, 075202 (2014).
202. Stefanucci, G., van Leeuwen, R. & Perfetto, E. In and out of equilibrium ab initio theory of electrons and phonons. *Phys. Rev. X* **13**, 031026 (2023).
203. Luo, Y., Park, J. & Bernardi, M. First-principles diagrammatic Monte Carlo for electron–phonon interactions and polaron. *Nat. Phys.* **21**, 1275 (2025).
204. Gilbert, S. J., Kurz, C., Greaves, R. G. & Surko, C. M. Creation of a monoenergetic pulsed positron beam. *Appl. Phys. Lett.* **70**, 1944–1946 (1997).
205. Kurz, C., Gilbert, S. J., Greaves, R. G. & Surko, C. New source of ultra-cold positron and electron beams. *Nucl. Instrum. Methods Phys. Res. B* **143**, 188–194 (1998).
206. Gilbert, S. J., Barnes, L. D., Sullivan, J. P. & Surko, C. M. Vibrational-resonance enhancement of positron annihilation in molecules. *Phys. Rev. Lett.* **88**, 043201 (2002).
207. Barnes, L. D., Gilbert, S. J. & Surko, C. M. Energy-resolved positron annihilation for molecules. *Phys. Rev. A* **67**, 032706 (2003).
208. Deutsch, M. Three-quantum decay of positronium. *Phys. Rev.* **83**, 866–867 (1951).
209. Surko, C. M., Passner, A., Leventhal, M. & Wysocki, F. J. Bound states of positrons and large molecules. *Phys. Rev. Lett.* **61**, 1831–1834 (1988).
210. Gribakin, G. F. Mechanisms of positron annihilation on molecules. *Phys. Rev. A* **61**, 022720 (2000).
211. Gribakin, G. F. in *New Directions in Antimatter Chemistry and Physics* (eds Surko, C. M. & Gianturco, F. A.) 22, 413 (Kluwer Academic, 2001).
212. Gribakin, G. F., Young, J. A. & Surko, C. M. Positron-molecule interactions: resonant attachment, annihilation, and bound states. *Rev. Mod. Phys.* **82**, 2557–2607 (2010).
213. Danielson, J. R., Arthur-Baidoo, E. & Surko, C. M. Improved positron-molecule binding energies and estimations using molecular parameters. *Phys. Rev. A* **111**, 042809 (2025).
214. Gribakin, G. F. & Lee, C. M. R. Positron annihilation in molecules by capture into vibrational Feshbach resonances of infrared-active modes. *Phys. Rev. Lett.* **97**, 193201 (2006).
215. Natisin, M. R., Danielson, J. R., Gribakin, G. F., Swann, A. R. & Surko, C. M. Vibrational feshbach resonances mediated by nondipole positron-molecule interactions. *Phys. Rev. Lett.* **119**, 113402 (2017).
216. Jones, A. C. L., Danielson, J. R., Natisin, M. R., Surko, C. M. & Gribakin, G. F. Ubiquitous nature of multimode vibrational resonances in positron–molecule annihilation. *Phys. Rev. Lett.* **108**, 093201 (2012).
217. Danielson, J. R., Jones, A. C. L., Natisin, M. R. & Surko, C. M. Modeling enhancement and suppression of vibrational Feshbach resonances in positron annihilation on molecules. *Phys. Rev. A* **88**, 062702 (2013).
218. Swann, A. R. et al. Effect of chlorination on positron binding to hydrocarbons: experiment and theory. *Phys. Rev. A* **104**, 012813 (2021).
219. Swann, A. R. & Gribakin, G. F. Effect of molecular constitution and conformation on positron binding and annihilation in alkanes. *J. Chem. Phys.* **153**, 184311 (2020).
220. Brownell, G. L. & Sweet, W. H. Localization of brain tumors with positron emitters. *Nucleonics* **11**, 40 (1953).
221. Pogossian, M. M. et al. A positron-emission transaxial tomograph for nuclear imaging (PETT). *Radiol* **114**, 89 (1975).
222. Alavi, A., Werner, T. J., Stępień, E. Ł & Moskal, P. Unparalleled and revolutionary impact of PET imaging on research and day to day practice of medicine. *Bio-Algorithms Med-Syst* **17**, 203 (2021).
223. Badawi, R. D. et al. First human imaging studies with the EXPLORER total-body PET scanner. *J. Nucl, Med.* **60**, 299 (2019).
224. Moskal, P. Positronium imaging. In *Proc. 2019 IEEE Nucl. Sci. Symp. Med. Imaging Conf. (NSS MIC)* 1 (IEEE, 2019).

225. Moskal, P., Jasińska, B., Stępień, E. Ł & Bass, S. D. Positronium in medicine and biology. *Nat. Rev. Phys.* **1**, 527 (2019).
226. Moskal, P. et al. Positronium imaging: history, current status, and future perspectives. *IEEE Trans. Radiat. Plasma Med. Sci.* **9**, 981 (2025).
227. Moskal, P. Positronium and quantum entanglement imaging: a new trend in positron emission tomography. In *Proc. 2021 IEEE Nucl. Sci. Symp. Med. Imaging Conf. (NSS MIC)* 16–23, 1 (IEEE, 2021).
228. Moskal, P. et al. Nonmaximal entanglement of photons from positron-electron annihilation demonstrated using a plastic PET scanner. *Sci. Adv.* **11**, eads3046 (2025).
229. Shibuya, K. et al. Oxygen sensing ability of positronium atom for tumor hypoxia imaging. *Commun. Phys.* **3**, 1 (2020).
230. Stepanov, P. et al. Interaction of positronium with dissolved oxygen in liquids. *Phys. Chem. Chem. Phys.* **22**, 5123 (2020).
231. Moskal, P. et al. Developing a novel positronium biomarker for cardiac myxoma imaging. *EJNMMI Phys.* **10**, 22 (2023).
232. Bass, S. D., Mariazzi, S., Moskal, P. & Stępień, E. Positronium physics and biomedical applications. *Rev. Mod. Phys.* **95**, 021002 (2023).
233. Moskal, P. & Stępień, E. Ł Positronium as a biomarker of hypoxia. *Bio-Algorithms Med-Syst* **17**, 311 (2021).
234. Takyu, S. et al. Positronium lifetime measurement using a clinical PET system for tumor hypoxia identification. *Nucl. Instrum. Methods Phys. Res. A* **1065**, 169514 (2024).
235. Vaupel, P., Flood, A. B. & Swartz, H. M. Oxygenation status of malignant tumors vs.normal tissues: critical evaluation and updated data source based on direct measurements with pO_2 microsensors. *Appl. Magn. Reson.* **52**, 1451 (2021).
236. Moskal, P. et al. Testing CPT symmetry in *ortho*-positronium decays with positronium annihilation tomography. *Nat. Commun.* **12**, 5658 (2021).
237. Moskal, P. et al. Positronium imaging with the novel multiphoton PET scanner. *Sci. Adv.* **7**, eabh4394 (2021).
238. Moskal, P. et al. Test of a single module of the J-PET scanner based on plastic scintillators. *Nucl. Instrum. Methods Phys. Res. A* **764**, 317 (2014).
239. Niedźwiecki, S. et al. J-PET: a new technology for the whole-body PET imaging. *Acta Phys. Pol. B* **48**, 1567 (2017).
240. Moskal, P. & Stępień, E. Ł Prospects and clinical perspectives of total-body PET imaging using plastic scintillators. *PET Clin.* **15**, 439 (2020).
241. Das, M. et al. Estimating the efficiency and purity for detecting annihilation and prompt photons for positronium imaging with J-PET using toy Monte Carlo simulation. *Bio-Algorithms Med-Syst* **19**, 87 (2023).
242. Moskal, P. et al. Positronium image of the human brain in vivo. *Sci. Adv.* **10**, eadp2840 (2024).
243. Moskal, P. et al. Feasibility study of the positronium imaging with the J-PET tomograph. *Phys. Med. Biol.* **64**, 055017 (2019).
244. Moskal, P. et al. Performance assessment of the 2γ positronium imaging with the total-body PET scanners. *EJNMMI Phys.* **7**, 44 (2020).
245. Steinberger, W. M. et al. Positronium lifetime validation measurements using a long-axial field-of-view positron emission tomography scanner. *EJNMMI Phys.* **11**, 76 (2024).
246. Huang, B. et al. High-resolution positronium lifetime tomography at clinical activity levels on the PennPET Explorer. *J. Nucl. Med.* **66**, 1464 (2025).
247. Mercolli, L. et al. First positronium lifetime imaging with scandium-44 on a long axial field-of-view PET/CT. *Front. Nucl. Med.* **5**, 1648621 (2025).
248. Qi, J. & Huang, B. Positronium lifetime image reconstruction for TOF PET. *IEEE Trans. Med. Imaging* **41**, 2848 (2022).
249. Chen, Z., An, L., Kao, C.-M. & Huang, H.-H. The properties of the positronium lifetime image reconstruction based on maximum likelihood estimation. *Bio-Algorithms Med-Syst* **19**, 1 (2023).
250. Huang, B. & Qi, J. High-resolution positronium lifetime tomography by the method of moments. *Phys. Med. Biol.* **69**, 24NT01 (2024).
251. Huang, B. et al. SPLIT: statistical positronium lifetime image reconstruction via time-thresholding. *IEEE Trans. Med. Imaging* **43**, 2148 (2024).
252. Huang, B. et al. Fast high-resolution lifetime image reconstruction for positron lifetime tomography. *Commun. Phys.* **8**, 181 (2025).
253. Huang, H.-H. et al. A statistical reconstruction algorithm for positronium lifetime imaging using time-of-flight positron emission tomography. *IEEE Trans. Radiat. Plasma Med. Sci.* **9**, 478 (2025).
254. Samanta, S., Sun, X., Li, H. & Li, Y. Feasibility study of positronium imaging using the NeuroEXPLORER (NX) brain PET scanner. In *2023 IEEE Nuclear Science Symposium, Medical Imaging Conference and International Symposium on Room-Temperature Semiconductor Detectors (NSS MIC RTSD)* 1 (IEEE, 2023).
255. Takyu, S. et al. Positron annihilation lifetime measurement with TOF-PET detectors: feasibility of Iodine-124 use. *Appl. Phys. Express* **16**, 116001 (2023).
256. Das, M. et al. First positronium imaging using 44Sc with the J-PET scanner: a case study on the NEMA-image quality phantom. *IEEE Trans. Radiat. Plasma Med. Sci.* **10**, 593 (2026).
257. Mercolli, L. et al. Phantom imaging demonstration of positronium. *EJNMMI Phys.* **12**, 80 (2025).
258. Mercolli, L. et al. In vivo positronium lifetime measurements with intravenous tracer administration and a long axial field-of-view PET/CT. In *IEEE Transactions on Radiation and Plasma Medical Sciences* https://doi.org/10.1109/TRPMS.2026.3687923 (2026).
259. Wenskat, M. et al. Vacancy dynamics in niobium and its native oxides and their potential implications for quantum computing and superconducting accelerators. *Phys. Rev. B* **106**, 094516 (2022).
260. Mohorovičić, S. Möglichkeit neuer elemente und ihre bedeutung für die astrophysik. *Astron. Nachr.* **253**, 94–108 (1934).
261. Ruark, A. E. Positronium. *Phys. Rev.* **68**, 278–278 (1945).
262. Wheeler, J. A. Polyelectrons. *Ann. NY Acad. Sci.* **48**, 219–238 (1946).
263. Feynman, R. P. The theory of positrons. *Phys. Rev.* **76**, 749–759 (1949).
264. Deutsch, M. Evidence for the formation of positronium in gases. *Phys. Rev.* **82**, 455–456 (1951).
265. Berko, S. & Plaskett, J. S. Correlation of annihilation radiation in oriented single metal crystals. *Phys. Rev.* **112**, 1877–1887 (1958).
266. Hotz, H. P., Mathiesen, J. M. & Hurley, J. P. Measurement of positron annihilation line shapes with a Ge(Li) detector. *Phys. Rev.* **170**, 351–355 (1968).
267. Hodges, C. H. Trapping of positrons at vacancies in metals. *Phys. Rev. Lett.* **25**, 284–287 (1970).
268. Lynn, K. G. & Goland, A. N. Observation of high momentum tails of positron-annihilation lineshapes. *Solid State Commun.* **18**, 1549–1552 (1976).

Acknowledgements

This material is based upon work supported by the Air Force Office of Scientific Research under award number FA8655-23-1-7057. F.T. and I.M. acknowledge funding from the Finnish Cultural Foundation through the Additional Million-euro Funding to Science programme, the Jane and Aatos Erkko Foundation (grant no. 250022), the Research Council of Finland (grant no. 349602) and the Business Finland Co-innovation programme (WIBASE — Wide Band-Gap Semiconductor Power Electronics, 5956/31/2024). D.G.G. acknowledges funding from the European Research Council (ERC) under the European Union's Horizon 2020 Research and Innovation Programme (grant agreement no. 101170577). S.W.H.E. acknowledges the MLZ, Garching, Germany, for providing positron beamtime at the PLEPS instrument of the NEPOMUC facility, for the study of perovskite solar cell layers (proposal no. 14598). A.K. gratefully acknowledges financial support from JSPS KAKENHI Grant-in-Aid for Scientific Research (S) (no. JP23H05462) and JST, CREST (grant no. JPMJCR23O3). P.M. and E.Ł.S. acknowledge funding from National Science Centre of Poland through grant nos. 2021/42/A/ST2/00423, 2021/43/B/ST2/02150, 2022/47/I/NZ7/03112, European Union within the Horizon Europe Framework Programme (ERC Advanced grant POSITRONIUM no. 101199807), the Ministry of Science and Higher Education through grant no. SPUB/SP/627733/2025 and the the SciMat and qLife Priority Research Areas budget under the programme Excellence Initiative — Research University at Jagiellonian University. F.S. acknowledges funding from FUTURE, an Energy Frontier Research Center funded by the US Department of Energy, Office of Science, Basic Energy Sciences.

Author contributions

The authors contributed equally to all aspects of the article.

Competing interests

P.M. is an inventor on a patent for positronium imaging described in this work (patent nos. (Poland) PL 227658, (Europe) EP 3039453 and (USA) US 9,851,456), filed (Poland) 30 August 2013, (Europe) 29 August 2014 and (USA) 29 August 2014; published (Poland) 23 January 2018, (Europe) 29 April 2020 and (USA) 26 December 2017. The other authors declare no competing interests.

Additional information

Peer review information *Nature Reviews Methods Primers* thanks Matthew McCluskey, Bang-Jiao Ye and the other, anonymous, reviewer(s) for their contribution to the peer review of this work.